Journal of Climate

GFDL's ESM2 global coupled climate-carbon Earth System Models Part II: Carbon system formulation and baseline simulation characteristics

--Manuscript Draft--

Manuscript Number:	
Full Title:	GFDL's ESM2 global coupled climate-carbon Earth System Models Part II: Carbon system formulation and baseline simulation characteristics
Article Type:	Article
Corresponding Author:	John Patrick Dunne, Ph D. National Oceanic and Atmospheric Administration Princeton, NJ UNITED STATES
Corresponding Author's Institution:	National Oceanic and Atmospheric Administration
First Author:	John Patrick Dunne, Ph D.
Order of Authors:	John Patrick Dunne, Ph D.
	Jasmin G John
	Robert W Hallberg
	Stephen M Griffies
	Elena N Shevliakova
	Ronald J Stouffer
	John P Krasting
	Lori T Sentman
	P. C. D. Milly
	Sergey L Malyshev
	Alistair J Adcroft
	William Cooke
	Krista A Dunne
	Matthew J Harrison
	Hiram Levy
	Andrew T Wittenberg
	Peter J Phillips
	Niki Zadeh
Abstract:	We describe the carbon system formulation and simulation characteristics of two new global coupled carbon-climate Earth System Models, ESM2M and ESM2G. These models demonstrate similar climate fidelity as the Geophysical Fluid Dynamics Laboratory's previous CM2.1 climate model as described in Part I while incorporating explicit and consistent carbon dynamics. The two models differ almost exclusively in the physical ocean component; ESM2M uses Modular Ocean Model version 4.1 with vertical pressure layers while ESM2G uses Generalized Ocean Layer Dynamics with a bulk mixed layer and interior isopycnal layers. On land, both ESMs include a new land model to interactively simulate vegetation distributions and functioning, including carbon cycling among vegetation, soil and atmosphere. In the ocean, both models include new biogeochemical algorithms including phytoplankton functional group dynamics with flexible stoichiometry. Preindustrial simulations are spun up to give stable, realistic carbon cycle mean and variability. Significant differences in simulation characteristics of these two models are described. Due to differences in oceanic ventilation rates (Part I) ESM2M has a stronger biological carbon pump but weaker

	northward implied atmospheric CO2 transport than ESM2G. The major advantages of ESM2G over ESM2M are: improved representation of surface chlorophyll in the Atlantic and Indian Oceans and thermocline nutrients and oxygen in the North Pacific. Additionally, changes in tree mortality parameters in ESM2G produced a more realistic carbon accumulation in vegetation pools. The major advantages of ESM2M over ESM2G are reduced nutrient and oxygen biases in the Southern and Tropical Oceans.
Suggested Reviewers:	Jonathan Gregory j.m.gregory@reading.ac.uk
	Chris Jones chris.d.jones@metoffice.gov.uk
	David Lawrence dlawren@ucar.edu
	Joellen Russell jrussell@email.arizona.edu
	Sandrine Bony sandrine.bony@lmd.jussieu.fr

Cover Letter
Click here to download Cover Letter: Carbon_doc_cover_letter.doc

UNITED STATES DEPARTMENT OF COMMERCE
National Oceanic and Atmospheric Administration/OAR
GEOPHYSICAL FLUID DYNAMICS LABORATORY
Princeton University Forrestal Campus
201 Forrestal Road
Princeton, New Jersey 08540-6649

February 22, 2012

TO: Dr. Anthony J. Broccoli
Editor, Journal of Climate
SUBJECT: GFDL ESM2M/ESM2G carbon cycle documentation manuscript

Dear Dr. Broccoli,

Following on from our recently accepted manuscript to *Journal of Climate*, "GFDL's ESM2 global coupled climate-carbon Earth System Models Part I: Physical formulation and baseline simulation characteristics", my co-authors and myself a proud to submit for your consideration the second part of this model documentation, "GFDL's ESM2 global coupled climate-carbon Earth System Models Part II: Carbon system formulation and baseline simulation characteristics" which provides the background biogeochemical description for GFDL's two coupled carbon Earth System Models that are being used as GFDL's contribution in support of the fifth phase of the Coupled Model Intercomparison Project in preparation for the fifth assessment of the Intergovernmental Panel on Climate Change. We are currently revising the companion manuscript describing the physical components based on the editor's and reviewers comments in order to hopefully publish the two contributions as a set. Together, we believe these manuscripts represent a critical contribution to the climate modeling field as they describe a new set of state of the art coupled carbon climate models and explore the role of ocean physical configuration on climate sensitivity.

Thank you very much for your consideration of this manuscript. Please let me know if there is anything I can do to expedite its consideration.

Sincerely,

John Dunne
Research Oceanographer
NOAA – Geophysical Fluid Dynamics laboratory
(609) 452-6596
email: John.Dunne@noaa.gov

GFDL's ESM2 global coupled climate-carbon Earth System Models Part II: Carbon system formulation and baseline simulation characteristics

John P. Dunne[a], Jasmin G. John[a], Robert W. Hallberg[a], Stephen M. Griffies[a], Elena N. Shevliakova[b], Ronald J. Stouffer[a], John P. Krasting[a,c], Lori T. Sentman[a], P. C. D. Milly[d], Sergey L. Malyshev[b], Alistair J. Adcroft[e], William Cooke[c], Krista A. Dunne[d], Matthew J. Harrison[a], Hiram Levy[a], Andrew T. Wittenberg[a], Peter J. Phillips[a], Niki Zadeh[c]

[a]National Oceanic and Atmospheric Administration/Geophysical Fluid Dynamics Laboratory, Princeton, New Jersey

[b]Department of Ecology and Evolutionary Biology, Princeton University, Princeton, New Jersey

[c]High Performance Technologies, Inc./GFDL, Princeton, New Jersey.

[d]U.S. Geological Survey, and National Oceanic and Atmospheric Administration/Geophysical Fluid Dynamics Laboratory, Princeton, New Jersey

[e]Program in Atmospheric and Oceanic Sciences, Princeton University, Princeton, New Jersey

Draft for submission to the Journal of Climate

February 28, 2012

Abstract

We describe the carbon system formulation and simulation characteristics of two new global coupled carbon-climate Earth System Models, ESM2M and ESM2G. These models demonstrate similar climate fidelity as the Geophysical Fluid Dynamics Laboratory's previous CM2.1 climate model as described in *Part I* while incorporating explicit and consistent carbon dynamics. The two models differ almost exclusively in the physical ocean component; ESM2M uses Modular Ocean Model version 4.1 with vertical pressure layers while ESM2G uses Generalized Ocean Layer Dynamics with a bulk mixed layer and interior isopycnal layers. On land, both ESMs include a new land model to interactively simulate vegetation distributions and functioning, including carbon cycling among vegetation, soil and atmosphere. In the ocean, both models include new biogeochemical algorithms including phytoplankton functional group dynamics with flexible stoichiometry. Preindustrial simulations are spun up to give stable, realistic carbon cycle mean and variability. Significant differences in simulation characteristics of these two models are described. Due to differences in oceanic ventilation rates (*Part I*) ESM2M has a stronger biological carbon pump but weaker northward implied atmospheric CO_2 transport than ESM2G. The major advantages of ESM2G over ESM2M are: improved representation of surface chlorophyll in the Atlantic and Indian Oceans and thermocline nutrients and oxygen in the North Pacific. Additionally, changes in tree mortality parameters in ESM2G produced a more realistic carbon accumulation in vegetation pools. The major advantages of ESM2M over ESM2G are reduced nutrient and oxygen biases in the Southern and Tropical Oceans.

Introduction

We describe the carbon system formulation and simulation characteristics of two new global coupled climate-carbon Earth System Models (ESMs; Fung et al., 2000) developed at the National Oceanic and Atmospheric Administration (NOAA) Geophysical Fluid Dynamics Laboratory (GFDL). Like global box models (e.g. Seigenthaler and Sarmiento, 1993; Figure 1A), ESMs represent major carbon reservoirs and fluxes (Figures 1B and 1C). As ESMs are extensions of climate models, they are based on mechanistic geophysical understanding with geographically explicit atmosphere, ocean, land and sea ice dynamics. To physical climate, ESMs add interactive carbon dynamics and associated chemistry and ecology to represent interactions on timescales from minutes to millennia and explore Earth System behavior at both equilibrium and in transient. ESMs resolve coupled climate-carbon responses to diverse anthropogenic perturbations such as fossil fuel emissions, agriculture and forestry, and aerosol chemistry within a single, self-consistent system.

Carbon in both the land and ocean has been implicated as having potentially strong responses and feedbacks to anthropogenic forcing. In a climate model with collapsing North Atlantic Overturning (Manabe and Stouffer, 1993), Sarmiento and LeQuere (1996) added simple ocean biogeochemistry to suggest that ocean carbon uptake and biological feedbacks exhibit high sensitivity and uncertainty. Friedlingstein et al. (2003) compared two early ESMs to show that CO_2 feedbacks were highly sensitive to representation of both the Southern Ocean and land vegetation and soil responses. Friedlingstein et al. (2006) compared a suite of early ESMs to suggest that land and ocean carbon responses each accounted for >100 PgC in emissions

62 uncertainty at an atmospheric CO_2 concentration of 700 ppm. Since then, much effort has
63 gone into developing fully coupled ESMs with long term stability in both climate and carbon
64 (e.g. Doney et al., 2006). One fundamental development has been the simulation of climate
65 without flux adjustment (e.g. Delworth et al., 2006; Reichler et al., 2008). Considerable
66 development has also taken place in both ocean biogeochemistry (e.g. Moore et al., 2004) and
67 land carbon (e.g. Thornton et al., 2007) models. Initial comparison of second generation ESMs
68 has shown large variability (e.g. Steinacher et al., 2010). More extensive comparison is
69 expected as part of the Coupled Model Intercomparison Project version 5 (CMIP5; Taylor et al.,
70 2011).

71 Our goal was to develop two ESMs with different ocean vertical coordinate and
72 dynamical/physical core while adhering to the climate fidelity of GFDL's CM2.1 (Delworth et al.,
73 2006). The primary benefit of our approach is to explore the sensitivity of ocean carbon and
74 heat uptake to anthropogenic forcing under fundamentally different frameworks describing
75 ocean dynamics. While the z-coordinate framework holds many benefits, the extreme
76 anisotropy of mixing and advection leads to spurious numerical mixing (Griffies et al., 2000;
77 Ilicak et al., 2012). While the isopycnal framework takes advantage of the relative ease of
78 motion between isopycnal layers, it loses resolution in the unstratified ocean. Comparison
79 between these formulations thus allows assessment of the relative and absolute fidelity of both
80 approaches in representing ocean physics, climate and biogeochemistry.

81 Dunne et al. (accepted; hereafter *Part I*), described the physical climate simulations of
82 both the z-coordinate (ESM2M) and isopycnal-coordinate (ESM2G) models, finding them of

similar overall fidelity but having distinct differences. Among these, while ESM2M warms in the interior and thickens the thermocline, ESM2G cools and thins the thermocline. While ESM2M has more thermocline ventilation, ESM2G has more bottom water ventilation. While ESM2M has an overly vigorous El Niño Southern Oscillation, that in ESM2G is rather weak.

First we describe the carbon cycle components in these two ESMs. We then discuss the initialization method used to obtain stable climate and carbon states. Finally, we present results from preindustrial control integrations with 1860 radiative forcing and potential vegetation (i.e. no land use) allowed to spin up for over 1000 years and then allowed to run with CO_2 interacting freely between the ocean-atmosphere-land system for another 600 years.

Model description

The physical components for the ESMs presented here are fully described in *Part I* with only the carbon system components described below.

Ocean Ecology and Biogeochemistry

The current GFDL ocean biogeochemical and ecological component is Tracers of Ocean Phytoplankton with Allometric Zooplankton code version 2.0 (TOPAZ2). A technical description of TOPAZ version 0 is available in Dunne et al. (2010). TOPAZ version 1 was discussed in Henson et al. (2009). TOPAZ2 includes 30 tracers to describe the cycles of carbon, nitrogen, phosphorus, silicon, iron, oxygen, alkalinity and lithogenic material as well as surface sediment calcite (Dunne et al., submitted). TOPAZ2 considers three explicit phytoplankton groups ('small', 'large', and

diazotrophic) that utilize a modified growth physiology after Geider et al. (1997) with Eppley (1972) temperature functionality and iron co-limitation with luxury uptake after Sunda and Huntsman (1997). 'Small' represent mostly prokaryotic picoplankton and nanoplankton, while 'large' represents diatoms, greens and other large eukaryotes. Diazotrophs represent facultative nitrogen fixers with nitrogen fixation inhibited by nitrate (NO_3), ammonia (NH_4) and oxygen (O_2). CO_2:NO_3:O_2 stoichiometry is 106:16:150 after Anderson (1995). N:P is based on optimal allocation after Klausmeier et al. (2004).

Phytoplankton loss and production of sinking detritus utilize the size-based relationship of Dunne et al. (2005) with mineral-driven penetration of sinking detritus (Klaas and Archer, 2002; Dunne et al., 2007). TOPAZ2 diagnoses plankton mineral formation of opal, calcite, and aragonite. TOPAZ2 includes seasonal time scale dissolved organic material and heterotrophic biomass with fixed N:P and multiannual dissolved organic material with variable N:P. Gas exchange of O_2 and CO_2 follows Najjar and Orr (1998). Nitrification is inhibited by light after Ward et al. (1982). TOPAZ2 includes second-order iron scavenging with ligand kinetics, lithogenic particle scavenging, water column denitrification under suboxia, and sediment denitrification after Middelburg et al. (1996). In the absence of both NO_3 and O_2, a respiration deficit is accumulated as negative O_2. TOPAZ2 includes external inputs of atmospheric nitrogen deposition (Horowitz et al., 2003), lithogenic dust and soluble iron (Fan et al., 2006), river nitrogen (Seitzinger et al., 2005), and river inputs of dissolved inorganic carbon, alkalinity and lithogenic material set to balance Holocene burial of calcite and lithogenic material (Dunne et al., 2007).

Land Vegetation and Carbon Cycle

The current GFDL land model (LM3) represents vegetation as 5 dynamically competing vegetation types: deciduous, coniferous, and tropical trees and warm and cold grasses. The five vegetation types are combinations of three characteristics: C3 versus C4 leaf physiology, leaf longevity (i.e. temperate cold-deciduous, tropical broadleaf, and coniferous evergreen), and allocation ratios among stems, roots, and leaves (i.e. trees versus grass). The tropical tree type can behave as evergreen or deciduous depending on the drought conditions. Vegetation height varies as a function of plant biomass across a continuum from shrubs through trees. All vegetation types have five carbon pools: leaves, fine roots, sapwood, heartwood, and labile. The sizes of all pools are modified daily through a set of allocation rules based on the amount of carbon accumulated in the biophysics module governing exchanges of water and CO_2 on fast time scales (30 minutes). LM3's photosynthesis is based on Farquhar et al. (1980) and Collatz et al. (1991, 1992). The relationship between stomatal conductance and net photosynthesis is based on Leuning (1995).

LM3 simulates changes in the vegetation carbon pools through phenology (e.g. leaf drop and emergence), natural mortality, and fire. Carbon loss from vegetation pools is deposited into two soil carbon pools that decompose at seasonal and multi-year timescales with the rates dependent on the amount of carbon, temperature, and water. Annual fire loss is proportional to fuel available and number of drought months. To ameliorate temperate biomass biases seen in initial ESM2M runs, ESM2G mortality was increased for evergreen coniferous trees from 0.015 a^{-1} to 0.0275 a^{-1} and for temperate deciduous trees from 0.015 a^{-1} to 0.025 a^{-1} while their branch-wood turnover rate was doubled.

One unique feature of LM3 is land-use heterogeneity in which each grid-cell is described as a combination of four land-use categories (tiles): undisturbed lands (i.e. "primary" or "potential"), croplands, pastures, and lands either previously harvested or used in agriculture (i.e. "secondary"). Each tile has its own carbon and physical state, above and belowground. In the absence of human disturbances, all grid-cells on land represent potential vegetation. These simulations were performed for the potential state of the vegetation and should more correctly be considered 'pre-human' rather than 'preindustrial' due to their lack of incorporation of land use history up to 1860. Nonetheless, for this work we retain the 'preindustrial' moniker for consistency with previous work.

Atmospheric CO_2

Atmospheric CO_2 was treated an explicit prognostic tracer exchanging CO_2 with land surface and ocean surface every 30 min and 2hr, respectively. For the initial phase of the long spin up (~1000 years) spin-up described here, this atmospheric CO_2 tracer was subjected to global, linear restoring to 286 ppm dry volume mixing ratio throughout the atmosphere with a restoring timescale of 1 year. This restoring approach was found to provide considerable advantages over the more direct, surface concentration override approach as it enabled the development of realistic diurnal and seasonal timescale CO_2 variability over the land which in turn influences plant growth and thus the land carbon inventory. Furthermore, it eliminated atmospheric CO_2 drift in the later phase of the spin up for both 'restored' CO_2 control and perturbed concentration scenarios, as well as scenarios with 'free' CO_2 (i.e. atmosphere exchanges CO_2 with ocean and land without any restoring and is free to evolve in 1860 control and emissions perturbation scenarios rather than being 'restored' to a pre-set value). The

model global average atmospheric CO_2 concentration is also used by the radiation code for the radiation calculation.

Initialization

To obtain the 1860 initial conditions for the climate model's control integration, a method similar to that described by Stouffer et al. (2004) is used. The model is initialized with present day conditions for ocean temperature (Locarnini et al., 2006) and salinity (Antonov et al., 2006) from the World Ocean Atlas 2005 in netCDF (Collier and Durack, 2006) and the ocean and sea ice run for a single year forced by atmospheric conditions from a CM2.1 control run. Biogeochemical tracers were initialized from observations from the World Ocean Atlas 2005 for nitrate, phosphate, silicate and oxygen (Garcia et al., 2006a; 2006b) and GLobal Ocean Data Analysis Project (GLODAP; Key et al., 2004) for alkalinity and dissolved inorganic carbon after subtracting off their anthropogenic carbon estimate. Sediment calcite is derived assuming steady state bottom water conditions and fluxes after Dunne et al. (submitted). All 1860 radiative forcings were included simultaneously at spin-up. The model was time integrated over 1000 model years in order to achieve a quasi-equilibrium defined by the net atmosphere-land and atmosphere-ocean fluxes being less than 0.1 PgC a^{-1} on the long term average. From this initial state, the 1860 control integrations and perturbation scenarios are begun. The land model was initialized off-line with CM2.1 climate forcing to obtain initial distribution of vegetation and soil carbon pools. After 500 hundred years, the last 50 years was used for offline soil equilibration after Shevliakova et al (2009) and the soil values reset.

Results

189 ***Initial Carbon Cycle Drift***

190 While our land carbon and sediment calcite components undergo offline initialization to
191 equilibrium, our ocean components require online equilibration in order to achieve our long
192 term 0.1 PgC a^{-1} quasi-equilibrium goal. Initial ALK and DIC inventory differences are due to
193 differences in total ocean volume (ESM2G has 0.5% more volume than ESM2M) with ESM2M's
194 relatively smooth bathymetry limited to 5500 m while ESM2G extends to 6000 m. Upon
195 initialization with preindustrial dissolved inorganic carbon (DIC) and present day alkalinity (ALK)
196 and nutrient distributions, both ESMs exhibit an initial pause before and then take up additional
197 CO_2 over the first few centuries before coming into equilibrium (Figure 2A and B). The drift in
198 ESM2G starts off strongly and takes up about 10 Pg more carbon than ESM2M, but also comes
199 into equilibrium more quickly. Both models have significant inter-annual variability, with that in
200 ESM2G being of longer period than ESM2M.

201 The rapid uptake of CO_2 in both these models over the first 300 years and long term DIC
202 inventory response relates to a complex interplay of factors including temperature drift,
203 accumulation of remineralized DIC in the tropics, loss of DIC in the deep Southern Ocean, and
204 long term equilibration of the calcite and nitrogen cycles. Because these models have
205 additional sources of carbon and ALK from rivers as well as sources and sinks of calcite from the
206 interaction with surface sediments, the ocean DIC inventory (Figure 2C) does not follow the
207 integrated gas exchange flux (Figure 2B) but rather decreases initially in both models before
208 stabilizing and then decreasing again in ESM2M versus slightly increasing before stabilizing and
209 then decreasing again in ESM2G. This differing long-term behavior between the two models,

210 also apparent in the ALK inventory (Figure 2D), is a result of the multi-millennial timescales
211 associated with the changing lysoclines as the models drift away from initial conditions and the
212 sediment seeks a new equilibrium. The ocean nitrogen inventory in these models (Figure 2E)
213 also undergoes a long term drift due to the imbalance between nitrogen supply from N_2
214 fixation, rivers, and atmospheric deposition versus loss from water column and sediment
215 denitrification, initially increasing, and then decreasing. As we describe below, this drift is due
216 to the common over-expression of pelagic suboxia in this class of models (Najjar et al., 2007).

217 ***Surface Ocean Biogeochemistry***

218 ESM2M and ESM2G share similar overall surface biogeochemical fidelity, but also
219 contrast in important ways. Surface observations are shown in Figure 3 for nitrate (NO_3; Garcia
220 et al., 2010b; Figure 3A), log chlorophyll (log(Chl); Figure 3D), the oceanic minus atmospheric
221 partial pressure of CO_2 (ΔpCO_2; Takahashi et al., 2009; Figure 3G), and phosphate (PO_4; Garcia et
222 al., 2010b; Figure 3J) are shown along with the corresponding model values in ESM2M (center;
223 Figures 3B, E, H, and K) and ESM2G (right; Figures 3C, F, I, and L). While both models capture
224 most regional variability in surface NO_3 (r^2 = 0.87 for ESM2M and r^2 = 0.91 for ESM2G), ESM2M
225 has a surplus compared to observations of 1.6 μM compared to the observed average of 5.1 μM
226 70°S-70°N, most notably in the Equatorial Pacific upwelling region, the Subpolar Front of the
227 Southern Ocean near 40°S, and the Subpolar North Atlantic. ESM2G, in contrast, has a muted
228 surplus in the Subpolar Front of the Southern Ocean near 40°S and minimal global scale bias (-
229 0.062 μM). Both models underestimate surface NO_3 in the Subpolar North Pacific, ESM2G more
230 severely.

ESM2M and ESM2G capture slightly more than half of log(Chl) spatial variability (r^2 = 0.54 for ESM2M; r^2 = 0.52 for ESM2G; Figures 3D-F). While neither model captures the high values in the north polar, coastal upwelling, and shelf regions, both models capture the transitions between oligotrophic subtropical gyres to mesotrophic, high nitrate regions. While much of these biases are attributable to the atmosphere, ESM2M better represents the tropical West Pacific, while ESM2G better represents the tropical Atlantic and Indian Oceans and subpolar regions of all oceans. We attribute these differences in surface NO_3 and Chl fidelity to differences in mixed layer dynamics (*Part I*) with ESM2G's capacity to represent shallow mixed layers allows phytoplankton maintaining high growth rates with lower chlorophyll than ESM2M. Strong shallow biases in minimum Southern Ocean mixed layer depths in both models (*Part I*) lead to locally low biases in surface NO_3 (ESM2G more severely than ESM2M) and high bias in Chl (ESM2M more severely than ESM2G).

Both models capture slightly more than half of spatial ΔpCO_2 variability (r^2 = 0.56 for ESM2M and r^2 = 0.55 for ESM2G; Figures 3G-I). The primary bias patterns include over expression of high ΔpCO_2 in the northerly and westward expressions of Equatorial Pacific upwelling, more so for ESM2G than ESM2M. ΔpCO_2 in both models is too low in the Northwest Pacific near 40°N, particularly in ESM2G, and too high in the Southern Ocean, particularly east of Australia and Argentina. While the global patterns in PO_4 (Figures 3J-L) bear much similarity with observations (r^2 = 0.87 for both models), ESM2M has a significant low bias in PO_4 (-0.087 μM) whereas ESM2G does not (0.0063 μM), opposite from their relative NO_3 biases.

Interior Ocean Biogeochemistry

252 Comparisons of biogeochemical distributions in the ocean interior highlight the limits of
253 these models' abilities to represent large scale ventilation patterns. Observations at 500 m are
254 shown in Figure 4 for dissolved oxygen (O_2; Garcia et al., 2010a; Figure 4A), phosphate (PO_4;
255 Figure 4D) and nitrate (NO_3; Figure 4G) along with the corresponding values in ESM2M (center;
256 Figures 4B, E, and H) and ESM2G (right; Figure4C, F, and I). While ESM2M reproduces 72% the
257 overall interior O_2 regional variability, it is overly ventilated in both the North Pacific and south
258 of 50°S and lacks ventilation of the Eastern Equatorial Pacific and Atlantic (Figure 4B). While
259 ESM2G represents the lack of oxygen ventilation in the North Pacific much better than ESM2M,
260 ESM2G reproduces slightly less (69%) of the variability overall as it exacerbates the ESM2M bias
261 of low ventilation of the tropical and southern subtropical oceans and Southern Ocean north of
262 60°S. In addition, ESM2G is overly ventilated south of 60°S. These patterns are mirrored in the
263 PO_4 patterns at 500 m (Figures 4D-F). Overall, ESM2M has an extremely low overall bias in O_2
264 and PO_4 at 500 m (-5.2 µM, and 0.005 µM, respectively), while ESM2G has a much larger
265 negative bias in O_2 (-32 µm) and positive bias in PO_4 (0.31 µM). Combined with their good
266 surface representation (Figures 3J-L), we infer these O_2 biases as due to under-ventilation
267 leading to excess accumulation of remineralization. Comparison of NO_3 at 500 m (Figures 4G-I),
268 highlights the severe implications of these ventilation biases for the nitrogen cycle as over-
269 expression of suboxia leads to excess denitrification and subsequent NO_3 deficiency in the
270 eastern tropical Pacific of ESM2M and even more so in ESM2G. This leads to both significant
271 global NO_3 drift (Figure 2E) and to ESM2G's relative surplus in surface PO_4 (Figure 3L).

272 Model fidelity for both Dissolved Inorganic Carbon (DIC) and excess alkalinity (ALK_{EXCESS} =
273 ALK-DIC; an approximation of the ocean buffering potential with respect to addition of CO_2 and

other acid) is demonstrated in Figure 5 through regional comparison of observed and modeled profiles. In the North Atlantic (Figure 5A), distributions of DIC and ALK_{EXCESS} have intermediate values throughout the water column, with ESM2G DIC values slightly elevated above 3000 m, and ESM2M DIC values slightly depressed below 700 m. ALK_{EXCESS} in both models, however, agrees well with observations in the upper water column but is slightly elevated below 700 m. In all tropical areas (Figure 5B), both models have elevated DIC at the base of the thermocline down to 2000 m consistent with their elevated phosphate and over expression of suboxia in the East Pacific (Figure 4), ESM2G more strongly and more into the thermocline than ESM2M. ALK_{EXCESS} is correspondingly depressed, though the observed structure is well-preserved. In the North Pacific (Figure 5C), ESM2G reproduces the DIC profile down to 700 m but has strongly depressed values below, while ESM2M underestimates DIC down to 2000 m with both models overestimating ALK_{EXCESS} through much of the water column. The differences in these deep patterns is due to the much higher Antarctic Bottom Water transport and lower ideal age distribution in ESM2G than ESM2M discussed in *Part I*. In the Southern Ocean (Figure 5D), DIC patterns similarly reflect these models' differing ventilation, with ESM2M reproducing the DIC profile extremely well down to 1200 m but having depressed values below, while ESM2G has elevated values in the 300-1400 m range and depressed values below. Both models exhibit slightly depressed ALK_{EXCESS} in this region above 1200 m and elevated values below.

Marine Ecosystem Functioning

The similar atmospheric coupling and identical biogeochemical algorithms but differing thermocline ventilation in these two models (*Part I*) results in roughly scaled marine ecological

functioning. Both models broadly center primary production on the equator with mid-latitude secondary maxima (Figures 6A-B) due to the combination of nutrient supply and equator-to-pole gradient in light and temperature. As a result of its more vigorous thermocline ventilation, ESM2M has higher total primary production than ESM2G in most ocean areas (Figure 6C). Patterns in large phytoplankton production (Figures 6D-F) are similar, except that the high productivity regions are more locally restricted to the site of ventilation. Exceptions to this general pattern include ESM2G's: 1) Southern Ocean high productivity ribbons shifted slightly southward, 2) a smaller Western Equatorial Pacific warm pool (*Part I*), and 3) California Current upwelling drawing from a shallower nutricline (Figure 5C). Nitrogen fixation patterns (Figures 6G-I) highlight the differing N:P stoichiometry in these models (Figure 4) with ESM2G (Figure 6G) having much higher nitrogen fixation in the North Pacific than ESM2M (Figure 6H) and 19% higher nitrogen fixation globally (ESM2G - 173 TgN a^{-1}; ESM2M - 146 TgN a^{-1}).

Comparison of zonally integrated metrics of the organic carbon pump (Figure 7A) illustrates both similarities and differences between ESM2M (solid) and ESM2G (dash). In both models, sinking particle export (black) follows large phytoplankton production (green) and NO_3-based production (light blue). Net community production (total primary production minus respiration; blue) and net phytoplankton production (total primary production minus grazing; red) exhibit more focused maxima in the high productivity regions. While the patterns of the two models are similar due to their similar atmospheric forcing, the ESM2M organic carbon pump is generally stronger than the ESM2G pump due to ESM2M's more vigorous thermocline ventilation (*Part I*). The similar biogeochemical response to atmospheric forcing is highlighted in net phytoplankton production (red) as upwelling-driven biomass accumulation and lateral

317 transport near the equator and convection-driven vertical transport at mid-latitudes. South of
318 40°S, while NO_3-based production (light blue) is nearly identical in these models, net
319 community production (blue) and particle export (black) are considerably lower in ESM2G than
320 ESM2M. This differing behavior in the Southern Ocean is due to their differences in depth-
321 resolution of light-inhibited nitrification. While ESM2M always has 10 m euphotic zone
322 resolution, ESM2G changes euphotic zone resolution based on stratification. Particularly in the
323 Southern Ocean, ESM2G layers directly below the mixed layer can thicken enough to relieve
324 light inhibition of nitrification and drive down ammonia.

325 The mineral pumps (Figure 7B) each highlight different controls dominating in different
326 regions. The silicon export (green) dominates in high productivity areas, the calcite pump (blue)
327 in the high temperature and saturation state tropics, the aragonite pump (black) in high
328 productivity tropical areas, and the lithogenic pump (red) focused in the northern hemisphere.
329 The similarity of the lithogenic pump between the two models is due to the fact that each was
330 given the same external supply from atmospheric deposition and river runoff. Note that while
331 the silicon pump is the strongest in terms of mass, all mineral pumps are important to the deep
332 organic carbon cycle due to the relative efficiency in mineral protection efficiency assumed for
333 calcite (0.070), aragonite (0.070), and lithogenic (0.065) mineral relative to silicon (0.026; Klaas
334 and Archer, 2002), and deep dissolution scales assumed for calcite and lithogenic mineral.

335 ***Land Vegetation and Carbon***

336 Both ESMS dynamically simulate vegetation characteristics as a function of climate and
337 atmospheric CO_2 concentration. To assess ESM2M and ESM2G fidelity with respect to land

dynamics, we compare three bulk characteristics critical to land-climate interactions: The distribution of vegetation types, total carbon storage, and the seasonal extremes of partitioning among different pools into leaves. We have combined information on the ESMs simulated vegetation type distribution with other vegetation characteristics (e.g. biomass, seasonality) to classify each of the land model grid-cells into one of the ten Aggregated Olson Ecotypes. Overall Ecotypes distributions (Olson et al., 1985) in both ESM2M (Figure 8B) and ESM2G (Figure 8C) compare well to observational estimates (Gibbs, 2006; Figure 8A) in representing the general distinction between warm grassland, tropical forest, cold grassland, hot sandy desert, deciduous forest, savanna, and coniferous forest, while tundra is under-represented in both models and permanently iced areas such as Greenland and Antarctica are specified. The models both over extend the areal coverage of tropical forest in South America and Africa at the expense of savanna, and over extend the areal coverage of hot sandy desert in Africa and South Asia at the expense of warm grassland. The models also exaggerate overestimate the westward extent of deciduous forest in North America and East Asia. Also in comparison to observational estimates (Gibbs, 2006; Figure 8D), both models (Figures 8E, F) overestimate both tropical and deciduous forest biomass, while due to the tuning differences, coniferous biomass is better represented in ESM2G than ESM2M.

As an essential ingredient for hydrological, radiative and carbon exchanges in the ESMs, we compare the ESM partitioning of biomass to leaves against the Normalized Difference Vegetation Index (NDVI) to evaluate whether the models make the correct amount of leaves at their seasonal extremes. Comparisons of NDVI in both models against the Moderate Resolution Imaging Spectroradiometer (MODIS) satellite (Figures 8G-L) illustrates strong agreement as

360 expected from the spectral calibration used in LM3 (Milly et al., submitted; *Part I*). The
361 climatological maximum comparison (Figures 8G-I) illustrates that the extent of permanent
362 deserts and semiarid regions is under represented in these models. This is because the low
363 precipitation extremes are not as extreme as in the satellite estimate. The climatological
364 minimum comparison (Figures 8J-L) illustrates the excellent observational agreement achieved
365 with these models in both the Northern Hemisphere snow line extent and transition between
366 coniferous and deciduous forests. However, the models appear to have overly high minimum
367 NDVI in tropical forest indicating a possible bias in lack of vegetation sensitivity to climate in
368 these regions.

369 Given that both ESMs share the same atmosphere and land model except for tree
370 mortality parameters, it is not surprising that the two models share nearly identical features.
371 Three main issues complicate evaluation of vegetation characteristics in these simulations. First,
372 most land vegetation and soil datasets are for present day conditions and include a substantial
373 footprint of past human activities. By design, the control experiments are performed for the
374 potential, preindustrial state. Second, most global datasets are derived from point
375 measurements extrapolated in space - often a product of complicated models themselves - with
376 high uncertainty. Third, as with many categorical variables, the challenge in evaluating a
377 modeled vegetation type distribution is that there is no exact correspondence between types of
378 vegetation used in the models and different vegetation classifications used to describe the state
379 of the land. We choose Olson Major World Ecosystem Types dataset for such comparison
380 because it was designed to reflect carbon content of different ecotypes as well degree of human
381 management of those ecosystems.

Atmospheric CO_2 Cycling

Combined land and ocean CO_2 fluxes into the atmosphere are shown in Figure 9. In the long term mean (Figures 9A, B) only ocean fluxes are apparent as land biomass is near equilibrium on the centennial scale. While ESM2M and ESM2G share similar overall CO_2 flux patterns, ESM2M has its strongest in-gassing north of Norway whereas that in ESM2G occurs in the Sea of Japan and Kuroshio Extension. ESM2M also shows strong in-gassing along the coast of Antarctica while ESM2G does not. Focusing on the monthly CO_2 flux variability (Figures 9C, D) nearly completely obscures the ocean due to the much higher land signal, with both models showing nearly identical patterns of intensely high fluxes in the tropical South American and African forests and savannas, and secondary zones of flux in tropical Asia, Eastern North America and Western Europe. As expected due to the primary driver of land variability fluxes by precipitation, the partitioning of variability between seasonal versus inter-annual modes of flux (Figures 9E, F) shows a strong dominance of seasonal variability except for the Equatorial Pacific and Indian Oceans as a consequence of the El Niño-Southern Oscillation (ENSO), especially for ESM2M where the ENSO signal extends to the Central Pacific, Indian and Atlantic Oceans. Additionally, ESM2G shows a strong inter-annual signal in the Southern Ocean while inter-annual signals in ESM2M for this region are moderate. ESM2G also shows a more inter-annual component in the Subpolar North Pacific. The local factors driving this variability are explored via the monthly air-land/sea CO_2 flux (F_{CO2}) correlation with monthly surface temperature (T_{Surf}) in Figures 9G, H. Strong positive F_{CO2}–T_{Surf} correlations are seen throughout the land but most particularly in South America, Australia and Southeast areas of Asia, Africa, and the United States as a function of the seasonal cycle in irradiance. In the ocean, these positive correlations

404 are restricted somewhat to the subtropics and Ross and Weddell Sea regions where seasonal
405 heating drive solubility-induced fluxes, whereas negative correlations are seen in the tropical
406 and Southern Ocean upwelling areas where remineralized CO_2 drives out-gassing during
407 upwelling of colder subsurface waters. This latter response is seen more prominently in ESM2G
408 than ESM2M due to its stronger pycnocline.

409 Comparison of time-averaged, zonally integrated, preindustrial air-sea fluxes (Figure
410 10A) of heat downward (PW deg^{-1} into the ocean; dash) and CO_2 upward (PgC deg^{-1} a^{-1}; solid)
411 and implied ocean transport (Figure 10B) of heat northward (PW; dash) and CO_2 southward (PgC
412 deg^{-1} a^{-1}; solid) serves to highlight both the differing dynamics controlling heat versus CO_2 fluxes
413 as well as the differences between ESM2M and ESM2G. Relative to heat, CO_2 flux is strong
414 south of 45°S, and meridionally broad in the tropics. As the Southern Ocean release is roughly
415 compensated by uptake south of 15°S, the tropical release is largely balanced northern mid-
416 latitude uptake. This divergence of CO_2 from heat is highlighted in the implied atmospheric CO_2
417 transport being northward at all latitudes north of 60°S whereas the implied ocean heat
418 transport is southward south of the equator (Figure 10B). While the two models have very
419 similar fluxes and transport for heat (ESM2G's northward heat transport being only slightly
420 stronger), ESM2G has a 28% stronger maximum CO_2 transport (0.97 PgC a^{-1}) than ESM2M (0.76
421 PgC a^{-1}) resulting from their differing extents of thermocline ventilation discussed in *Part I*. In
422 ESM2M, CO_2 locally remineralized in the subsurface tends to ventilate back to the atmosphere
423 during winter convection at northern mid-latitudes while ESM2G maintains a stronger biological
424 pump and more uptake at sub-polar latitudes.

425 ***Atmospheric CO_2 Variability***

426 The atmospheric signatures of regional land and ocean CO_2 fluxes are presented in
427 Figure 11. At the regional scale, surface atmospheric CO_2 anomalies from the global mean
428 (Figures 11A, B) are driven at the regional scale by the dominance of land variability over ocean
429 variability (Figure 9) and exhibit broad maxima centered on the productive land areas that
430 spread over the marine areas particularly in the tropics. These features are a consequence of
431 the well-characterized atmospheric CO_2 rectification effect (Denning et al., 1995) such that at
432 night when the boundary layer is thin, the land undergoes net respiration and CO_2 increases
433 dramatically, while during the day when the land undergoes photosynthesis, the boundary layer
434 thickens as the land heats and CO_2 concentrations decrease to a lesser degree. At the global
435 scale, these anomalies also demonstrate a general marine gradient of decreasing CO_2 from
436 south to north as a consequence of the general southward transport of CO_2 in the ocean (Figure
437 10). Temporal changes in global mean surface CO_2 anomalies are highly correlated with
438 temporal changes at regional scales (Figures 11A, B) except for directly above the regions of
439 high land productivity. Because of this globally synoptic behavior, local CO_2 variability in such
440 distant places as Antarctica (black in Figures 11E, F) and Greenland (blue in Figures 11E, F) is
441 largely co-incident (r^2=0.81 for ESM2M and r^2=0.84 in ESM2G) with concentrations at Antarctica
442 approximately 1.2 ppm higher than at Greenland in ESM2M and 1.3 ppm higher in ESM2G.

443 We compare ESM2M and ESM2G with observations of the amplitude of the marine
444 seasonal CO_2 cycle (Figure 12) to demonstrate the relative dampening of the latitudinal signal
445 long recognized in the atmospheric CO_2 cycle (Fung et al., 1987), with ESM2G suffering slightly

446 more so from this bias than ESM2M due to ESM2G's relatively strong seasonal cycle in the
447 tropics (*Part I*, Figure 7 therein). The cause of the damped meridional gradient is twofold: 1)
448 under predicting the strength of the seasonal cycle in the northern boreal forests and 2) an
449 overly enhanced seasonal cycle in the Amazon. In northern boreal regions, our models initiate
450 CO_2 drawdown approximately one month earlier than observations and return CO_2 to higher,
451 winter values approximately two months early. While our model underestimates maximum
452 NDVI in Siberian forests (Figures 8J-L), our net primary productivity cycle matches that in
453 satellite based estimates (Randerson et al., 1997; not shown), leading us to suspect the
454 underlying net ecosystem production bias to be rather in the seasonality of respiration. The
455 Amazon bias is due to a combination of the overall low Amazon precipitation, relative
456 intensification of length of the dry season, lack of seasonally intense cloud cover, and related
457 soil hydrology biases common to this class of model (*Part I*, Figure 6 therein). These factors
458 result in a modeled Amazonian seasonal CO_2 flux cycle synchronous with the African and
459 Oceania rainforests giving strong CO_2 seasonality extending to the South Pole with net
460 community production driven by precipitation - whereas in observations, a combination of
461 intense cloud cover during the high precipitation season and a lack of water stress at other
462 times results in an Amazonian cycle of opposing phase counteracting the CO_2 signature of the
463 seasonal cycle in the other rainforests.

464 To further quantify atmospheric CO_2 variability, we show as insets in Figure 12 the
465 temporal variability spectrum at the long term Barrow, Alaska, Mauna Loa, and South Pole
466 monitoring stations (detrended; black) compared to ESM2M (red) and ESM2G (green). At high
467 northern latitudes (e.g. Barrow), both models underestimate the annual cycle and sub-annual

cycle, but have approximately correct inter-annual variability. At mid-northern latitudes (e.g. Mauna Loa), both models overestimate inter-annual variability (ESM2M more so than ESM2G) and underestimate the seasonal cycle. In the southern hemisphere, both models over estimate variability at both annual and inter-annual time-scales, with ESM2M exhibiting more bias on interannual timescales, and ESM2G exhibiting more bias on annual timescales as both models degas CO_2 from the Southern Ocean in the Austral Summer. This signal is stronger in ESM2G than ESM2M, consistent with its larger warm sea surface temperature bias in the Southern Ocean described in *Part I*.

Overall Land and Ocean Biosphere Representation in GFDL's ESM2 Class of Models

Overall, the models demonstrate the ability to represent a wide range of coupling between climate and the carbon cycle. Having described all of the various components of these models, we now turn back to the comparison of carbon inventory and flux estimates in Figure 1. Both models demonstrate excellent agreement with previous estimates in terms of the partitioning of carbon between the various reservoirs, though the land vegetation is quite a bit higher and the ocean biota quite a bit lower than those in the observational synthesis and box model analysis of Siegenthaler and Sarmiento (1993) which is used as a quasi-consensus estimate used in the IPCC Fourth Assessment (Randall et al., 2007). There remains a great deal of uncertainty in these estimates, however. While the Sabine et al. (2004) land gross primary production estimate (120 PgC a^{-1}) given in Figure 1 is higher than the original Siegenthaler and Sarmiento (1993) estimate (100 PgC a^{-1}) and similar to the Beer et al. (2010) estimate of 123 PgC a^{-1}, it is well below the latest best guess of 150–175 PgC a^{-1} from the recent observational

estimates (Welp et al., 2011). Both ESM2M (141 PgC a^{-1}) and ESM2G (143 PgC a^{-1}) estimates are between these two studies. The global biomass in both models (1044 PgC in ESM2M and 838 PgC in ESM2G) compares well to preindustrial estimates of 924 – 1080 PgC (Bazilevich and Rodin, 1971; Adams et al., 1990). Note also that the Siegenthaler and Sarmiento (1993) biomass is for preindustrial (~1850s) which incorporates significant historical land use and is expected to be lower than preindustrial estimates.

Ocean primary productivity is higher than the Siegenthaler and Sarmiento (1993) value (50 PgC a^{-1}) in both ESM2M (82 PgC a^{-1}) and ESM2G (68 PgC a^{-1}), and at the upper end of the range of global productivity estimates (36-78 PgC a^{-1}) given in the comparative analysis of Carr et al. (2006) and much higher than the model range given in Steinacher et al. (2010; 24-49 PgC a^{-1}). However, ESM2M (8.0 PgC a^{-1}) and ESM2G (5.4 PgC a^{-1}) are within the range of modeled particulate organic carbon export (5.0-9.1 PgC a^{-1}) in Steinacher et al. (2010), indicating that the primary production differences are largely a function of differing recycling efficiency between these studies. We have split the ESM2M and ESM2G carbon export across 100 m in Figure 1 into three terms: dissolved transport which is much smaller than in Siegenthaler and Sarmiento (1993); sinking particulate organic carbon export (bold arrow) which is higher than Siegenthaler and Sarmiento for ESM2M, but of similar magnitude in ESM2G; and combined organic particle (phytoplankton, zooplankton and bacteria) transport and aragonite and calcite sinking. Combined, these export fluxes give an inferred ventilation of the upper 100 m in ESM2M (98 PgC a^{-1}) in excellent agreement with Siegenthaler and Sarmiento (1993; 100 PgC a^{-1}) while that in ESM2G (80 PgC a^{-1}) is moderately lower. Note that since these ESMs do not include an explicit representation of organic carbon cycling in rivers, our net atmospheric flux into land is

511 zero, and the river runoff flux of DIC and ALK is specified with a 1:2 ratio to balance calcite burial
512 at steady state. This steady state is yet unachieved in our control runs as ESM2M with 642 PgC
513 in surface sediment calcite is gaining 0.05 PgC a^{-1} and ESM2G with 469 PgC in surface sediment
514 calcite is gaining 0.12 PgC a^{-1}. Assessment of the sensitivity of the sediment calcite inventory to
515 ocean acidification will thus require careful attention to the behavior of the control runs for
516 comparison.

517

518 **Conclusions**

519 Representation of the carbon cycle in GFDL's climate models has exposed a wide range
520 of sensitivities beyond those normally focused upon in analysis of climate. As discussed above,
521 many of the biases relative to observationally based estimates are common to both models. On
522 land, the models over-estimate the seasonal flux of CO_2 to the atmosphere in the tropics, and
523 under estimate it in boreal high latitudes (e.g. Figure 12). In the tropics, we attribute this bias to
524 a combination of the physical model's inability to represent the actual radiative and hydrological
525 cycle in the Amazon (not shown), and the enhanced northward extent of seasonal productivity
526 in the Sahel (Figures 8G-I). In the ocean, both models over estimate surface chlorophyll (Figures
527 3D-F) and the extent of interior suboxia (Figures 4A-C). The relative equatorward restriction of
528 the subtropical gyre oligotrophic region is a cause of concern for the representation of
529 ecological biomes and over estimation of mid-latitude nutrient and oxygen ventilation, both of
530 which are better represented in ESM2G than ESM2M. While not directly connected to the
531 surface biogeochemistry, the oxygen bias has severe implications for the ability to represent

hypoxia and denitrification in the tropics (Figure 5B), and to achieve a steady state budget for global alkalinity (Figure 2D) and nitrogen (Figures 2E, 4G-I). Efforts to address these biases are ongoing. Overall, however, the models' very good representation of surface nutrients and ΔpCO_2 (Figure 3) and interior excess alkalinity (dashed lines in Figure 5), in combination with the general agreement with physical metrics of transport and ventilation discussed in *Part I* (Dunne et al., accepted), give us confidence that the models should have good fidelity in representing ocean carbon uptake and acidification sensitivity under anthropogenic emissions.

The primary biogeochemical differences between ESM2M and ESM2G relate to their differing physical representations of thermocline ventilation, and the magnitude of Antarctic Bottom Water (AABW) penetration into the deep Pacific as discussed in *Part I* (Dunne et al., accepted). In ESM2G, lower thermocline ventilation leads to a lower productivity (Figures 1, 6), higher Southern Ocean and tropical thermocline DIC (Figures 5B, D), and larger northward atmospheric CO_2 transport (Figure 10B) than in ESM2M. In the North Pacific, higher AABW ventilation of the deep North Pacific in ESM2G leads to deficit of DIC relative to ESM2M and observations in deep waters, while higher thermocline ventilation in ESM2M leads to deficit of DIC relative to ESM2G and observations in the upper water column (Figure 5C).

In summary, we find ESM2M and ESM2G of similar overall fidelity, both capable of representing the major carbon inventories and fluxes in a prognostic earth system context. The models are capable of simulating realistic levels of biogeochemical function (Figure 1) and global atmospheric CO_2 variability (Figures 11, 12) without significant drift (Figure 2). Regionally, the models are capable of representing factors controlling productivity and net CO_2

553 exchanges between the atmosphere and both land and ocean (Figures 9, 10), though regional
554 biases in variability do exist. The major advantages of ESM2G over ESM2M are improved
555 representation of the subtropical, oligotrophic gyre structure in general and specifically lack of
556 nutrient oxygen ventilation in the Northeast Pacific. The major advantages of ESM2M over
557 ESM2G are in reduced tropical nutrient trapping and suboxia biases - also due to the enhanced
558 thermocline ventilation in ESM2M. While some ocean interior and sediment calcite drifts
559 continue through our control runs, the surface fluxes and interior budgets for both models are
560 balanced to within a 0.1 PgC a^{-1} tolerance in order to provide a strong signal to noise ratio under
561 conditions of anthropogenic CO_2 emissions with Intergovernmental Panel on Climate Change
562 (IPCC) Fourth Assessment consensus estimate for ocean CO_2 uptake in the 1990s at 2.2 ± 0.4
563 PgC a^{-1} (Denman et al., 2007; Table 7.1 therein). We expect the model differences described
564 here will drive much of the ocean carbon uptake and acidification sensitivity under
565 anthropogenic CO_2 emissions between ESM2M and ESM2G. Such simulations and analyses are
566 ongoing as part of GFDL's contribution to the IPCC Fifth Assessment.

567

568 **Acknowledgements**

569 Discussions with Inez Fung, Scott Doney and Chris Jones helped inform the experimental
570 design of these simulations. Charles Stock and Robbie Toggweiler provided extremely helpful
571 reviews of the early manuscript.

572

573

574 **References**

575 Adams , J.M. , H. Faure , L. Taure-Denard , J. M. McGlade , and H. I. Woodward , 1990: Increase
576 in terrestrial carbon storage from the last glacial maximum to the present. *Nature*, **348**, 711 –
577 714.

578 Anderson, L. A., 1995: On the hydrogen and oxygen content of marine phytoplankton, *Deep-Sea*
579 *Res. I*, **42**, 1675-1680.

580 Antonov, J. I., R. A. Locarnini, T. P. Boyer, A. V. Mishonov, and H. E. Garcia, 2006. World Ocean
581 Atlas 2005, Volume 2: Salinity. S. Levitus, Ed. NOAA Atlas NESDIS 62, U.S. Government Printing
582 Office, Washington, D.C., 182 pp.

583 Bazilevich, N. I. and L. Y. Rodin, 1971: Geographical regularities in productivity and the
584 circulation of chemical elements in the Earth's main vegetation types. *Soviet Geography: Review*
585 *and Translation*, **12**: 24-53.

586 Beer, C., M. Reichstein, E. Tomelleri, P. Ciais, M. Jung, N. Carvalhais, C. Rödenbeck, M. A. Arain,
587 D. Baldocchi, G. B. Bonan, A. Bondeau, A. Cescatti, G. Lasslop, A. Lindroth, M. Lomas, S.
588 Luyssaert, H. Margolis, K. W. Oleson, O. Roupsard, E. Veenendaal, N. Viovy, C. Williams, F. I.
589 Woodward, and D. Papale, 2010: Terrestrial gross carbon dioxide uptake: Global distribution and
590 covariation with climate, *Science*, **329**, 834–838.

591 Carr, M.-E., M. Friedrichs, M. Schmeltz, M. N. Aita, D. Antoine, K. R. Arrigo, I. Asanuma, O.
592 Aumont, R. Barber, M. Behrenfeld, R. Bidigare, E. Buitenhuis, J. Campbell, A. Ciotti, H. Dierssen,
593 M. Dowell, J. Dunne, W. Esaias, B. Gentili, S. Groom, N. Hoepffner, J. Ishizaka, T. Kameda, C.

LeQuere, S. Lohrenz, J. Marra, F. Melin, K. Moore, A. Morel, T. Reddy, J. Ryan, M. Scardi, T. Smyth, K. Turpie, G. Tilstone, K. Waters, Y. Yamanaka (2006) A comparison of global estimates of primary production from ocean color. *Deep-Sea Res. II*, **53**, 741-770.

Collatz G.J., J. T. Ball, C. Grivet, and J. A. Berry, 1991: Physiological and environmental regulation of stomatal conductance, photosynthesis and transpiration: a model that includes a laminar boundary layer. *Agricultural and Forest Meteorology*, **54**, 107-136.

Collatz, G.J., M. Ribas-Carbo, and J. A. Berry, 1992: A coupled photosynthesis - stomatal conductance model for leaves of C4 plants. *Australian Journal of Plant Physiology*, **19**, 519-538.

Collier, M. A., and P. Durack, 2006: CSIRO netCDF version of the NODC World Ocean Atlas 2005. Commonwealth Scientific and Industrial Research Organisation, *Marine and Atmospheric Research Paper 15*, 1–45 pp.

Delworth, T. D., A. J. Broccoli, A. Rosati, R. J. Stouffer, V. Balaji, J. A. Beesley, W. F. Cooke, K. W. Dixon, J. Dunne, K. A. Dunne, J. W. Durachta, K. L.Findell, P. Ginoux, A. Gnanadesikan, C. T. Gordon, S. M. Griffies, R. Gudgel, M. J. Harrison, I. M. Held, R.S. Hemler, L. W. Horowitz, S. A. Klein, T. R. Knutson, P. J. Kushner, A. R. Langenhorst, H.-C. Lee, S.-J. Lin, J. Lu, S. L. Malyshev, V. Ramaswamy, J. Russell, M. D. Schwarzkopf, E. Shevliakova, J. J. Sirutis, M. J. Spelman, W. F. Stern, M. Winton, A. T. Wittenberg, B. Wyman, F. Zeng, and R. Zhang, 2006: GFDL's CM2 global coupled climate models-Part I: Formulation and simulation characteristics. *J. Clim*., **19**, 643-674.

Denman, K.L., G. Brasseur, A. Chidthaisong, P. Ciais, P.M. Cox, R.E. Dickinson, D. Hauglustaine, C. Heinze, E. Holland, D. Jacob, U. Lohmann, S Ramachandran, P.L. da Silva Dias, S.C. Wofsy and X.

614 Zhang, 2007: Couplings Between Changes in the Climate System and Biogeochemistry. In:
615 *Climate Change 2007: The Physical Science Basis. Contribution of Working Group I to the Fourth*
616 *Assessment Report of the Intergovernmental Panel on Climate Change* [Solomon, S., D. Qin, M.
617 Manning, Z. Chen, M. Marquis, K.B. Averyt, M.Tignor and H.L. Miller (eds.)]. Cambridge
618 University Press, Cambridge, United Kingdom and New York, NY, USA.

619 Denning, A. S., I. Y. Fung, and D. A. Randall, 1995: Latitudinal gradient of atmospheric CO2 due
620 to seasonal exchange with land biota, *Nature*, **376**, 240–243.

621 Doney, S. C., K. Lindsay, I. Fung, and J. John, 2006: Natural variability in a stable, 1000-yr global
622 coupled climate-carbon cycle simulation. J. Clim., 19, 3033-3054.

623 Dunne, J. P., R. A. Armstrong, A. Gnanadesikan, J. L. Sarmiento, and R. D. Slater, 2005: Empirical
624 and mechanistic models for particle export ratio. *Global Biogeochem. Cycles*, **18**,
625 doi:10.1029/2004GB002390.

626 Dunne, J. P., J. L. Sarmiento, and A. Gnanadesikan, 2007: A synthesis of global particle export
627 from the surface ocean and cycling through the ocean interior and on the seafloor, *Global*
628 *Biogeochem. Cycles*., **21**, doi:10.1029/2006GB002907.

629 Dunne, J. P., A. Gnanadesikan, J. L. Sarmiento and R. D. Slater, 2010 Technical description of the
630 prototype version (v0) of Tracers of Phytoplankton with Allometric Zooplankton (TOPAZ) ocean
631 biogeochemical model as used in the Princeton IFMIP model, *Biogeosciences Supplement*, **7**,
632 3593.

633 Dunne, J. P., J. R. Toggweiler, and B. Hales, submitted: Global calcite cycling constrained by
634 sediment preservation controls. Glob. Biogeochem. Cycles.

635 Dunne, J. P., J. G. John, A. J. Adcroft, S. M. Griffies, R. W. Hallberg, E. N. Shevliakova, R. J.
636 Stouffer, W. Cooke, K. A. Dunne, M. J. Harrison, J. P. Krasting, H. Levy, S. L. Malyshev, P. C. D.
637 Milly, P. J. Phillipps, L. A. Sentman, B. L. Samuels, M. J. Spelman, M. Winton, A. T. Wittenberg, N.
638 Zadeh, accepted: GFDL's ESM2 global coupled climate-carbon Earth System Models Part I:
639 Physical formulation and baseline simulation characteristics, J. Climate.

640 Eppley R. W., 1972: Temperature and phytoplankton growth in the sea. *Fish. Bull*., **70**, 1063-
641 1085.

642 Fan, S.-M., W. Moxim, and H. Levy II, 2006: Aeolian input of bioavailable iron to the ocean.
643 *Geophys. Res. Lett.,* **33**, L07602, DOI:10.1029/2005GL024852.

644 Farquhar, G.D., S. von Caemmerer, and J.A. Berry, 1980: A Biochemical Model of Photosynthetic
645 CO2 Assimilation in Leaves of C3 species. *Planta*, **149**, 78-90.

646 Friedlingstein P., Dufresne J.-L., Cox P. M., and Rayner P., 2003: How positive is the feedback
647 between climate change and the carbon cycle? *Tellus*, **55**, 692-700.

648 Friedlingstein P., P. Cox, R. Betts, L. Bopp, B. W. Von, V. Brovkin, P. Cadule, S. Doney, M. Eby, I.
649 Fung, G. Bala, J. John, C. Jones, F. Joos, T. Kato, M. Kawamiya, W. Knorr, K. Lindsay, H. D.
650 Matthews, T. Raddatz, P. Rayner, C. Reick, E. Roeckner, K. G. Schnitzler, R. Schnur, K. Strassmann,
651 A. J. Weaver, C. Yoshikawa, and N. Zeng, 2006: Climate-carbon cycle feedback analysis: Results
652 from the C^4MIP model intercomparison, *J. Clim*., **19**, 3337-3353.

Fung, I., C. J. Tucker, and K. C. Prentice, 1987: Application of Advanced Very High Resolution Radiometer Vegetation Index to study atmosphere-biosphere exchange of CO_2. *J. Geophys. Res.*, **92**, 2999-3015.

Fung, I., P. Rayner, and P. Friedlingstein, 2000: Full-form earth system models: Coupled carbon-climate interaction experiment (the flying leap). IGBP Global Change Newslet., 41, 7–8.

Garcia, H. E., R. A. Locarnini, T. P. Boyer, J. I. Antonov, O. K. Baranova, M. M. Zweng, and D. R. Johnson, 2010a: World Ocean Atlas 2009, Volume 3: Dissolved Oxygen, Apparent Oxygen Utilization, and Oxygen Saturation. S. Levitus, Ed. NOAA Atlas NESDIS 70, U.S. Government Printing Office, Washington, D.C., 344 pp.

Garcia, H. E., R. A. Locarnini, T. P. Boyer, and J. I. Antonov, 2006a. World Ocean Atlas 2005, Volume 3: Dissolved Oxygen, Apparent Oxygen Utilization, and Oxygen Saturation. S. Levitus, Ed. NOAA Atlas NESDIS 63, U.S. Government Printing Office, Washington, D.C., 342 pp.

Garcia, H. E., R. A. Locarnini, T. P. Boyer, and J. I. Antonov, 2006b: World Ocean Atlas 2005, Volume 4: Nutrients (phosphate, nitrate, silicate). S. Levitus, Ed. NOAA Atlas NESDIS 64, U.S. Government Printing Office, Washington, D.C., 396 pp.

Garcia, H. E., R. A. Locarnini, T. P. Boyer, J. I. Antonov, O. K. Baranova, M. M. Zweng, and D. R. Johnson, 2010a. World Ocean Atlas 2009, Volume 3: Dissolved Oxygen, Apparent Oxygen Utilization, and Oxygen Saturation. S. Levitus, Ed. NOAA Atlas NESDIS 70, U.S. Government Printing Office, Washington, D.C., 344 pp.

672 Garcia, H. E., R. A. Locarnini, T. P. Boyer, J. I. Antonov, M. M. Zweng, O. K. Baranova, and D. R.
673 Johnson, 2010b: World Ocean Atlas 2009, Volume 4: Nutrients (phosphate, nitrate, silicate). S.
674 Levitus, Ed. NOAA Atlas NESDIS 71, U.S. Government Printing Office, Washington, D.C., 398 pp.

675 Geider, R. J., H. L. MacIntyre, and T. M. Kana, 1997: A dynamic model of phytoplankton growth
676 and acclimation: Responses of the balanced growth rate and chlorophyll a: carbon ratio to light,
677 nutrientlimitation and temperature. *Mar. Ecol. Prog. Ser.*, **148**, 187-200.

678 Gibbs, H. K., 2006: Olson's Major World Ecosystem Complexes Ranked by Carbon in Live
679 Vegetation: An Updated Database Using the GLC2000 Land Cover Product. NDP-017b. doi:
680 10.3334/CDIAC/lue.ndp017.2006.

681 Gibson, J.K., P. Kallberg, S. Uppala, A. Hernandez, A. Nomura, and E. Serrano, 1997: ERA
682 Description. Vol 1. ECMWF Re-analysis Project Rep. Series, European Centre for Medium-Range
683 Weather Forecasts, Reading, United Kingdom, 66 pp.

684 Griffies, S. M., R. C. Pacanowski, and R. W. Hallberg, 2000: Spurious diapycnal mixing associated
685 with advection in a z-coordinate ocean model. *Mon. Weath. Rev*., **128**, 538-564.

686 Henson, S. A., J. P. Dunne, and J. L. Sarmiento, 2009: Decadal variability in North Atlantic
687 phytoplankton blooms. *J. Geophys. Res*., **114**, C04013, doi:10.1029/2008JC005139.

688 Horowitz, L. W., S Walters, D. L. Mauzerall, L. K. Emmons, P. J. Rasch, C. Granier, X. Tie, J. F.
689 Lamarque, M. Schulz, G. S. Tyndall, I. Orlanski, and G. P. Brasseur, 2003: A global simulation of
690 tropospheric ozone and related tracers: description and evaluation of MOZART, version 2. *J.*
691 *Geophys. Res.*, **108**, 4784, DOI:10.1029/2002JD002853.

692 Ilicak, M., A. Adcroft, S. M. Griffies, and R. W. Hallberg, 2012: Spurious dianeutral mixing and the
693 role of momentum closure. *Ocean Modelling*. DOI:10.1016/j.ocemod.2011.10.003. 11/11.

694 Key, R. M., Kozyr, A., Sabine, C. L., Lee, K., Wanninkhof, R., Bullister, J., Feely, R. A., Millero, F.,
695 Mordy, C., and Peng, T.-H., 2004: A global ocean carbon climatology: results from GLODAP,
696 *Global Biogeochem.Cycles.*, **18**, GB4031, doi:10.1029/2004GB002247.

697 Klaas, C., and D. Archer, 2002: Association of sinking organic matter with various types of
698 mineral ballast in the deep sea: Implications for the rain ratio, *Global Biogeochem. Cycles*, **16**,
699 1116, doi:10.1029/2001GB001765.

700 Klausmeier, C.A., E. Litchman, T. Daufresne and S.A. Levin. 2004. Optimal N:P stoichiometry of
701 phytoplankton. *Nature*, **429**, 171-174.

702 Leuning, R., 1995: A critical appraisal of a combined stomatal-photosynthesis model for C3
703 plants. *Plant, Cell and Environment*, **18**, 339–355.

704 Locarnini, R. A., A. V. Mishonov, J. I. Antonov, T. P. Boyer, H. E. Garcia, O. K. Baranova, M. M.
705 Zweng, and D. R. Johnson, 2010. World Ocean Atlas 2009, Volume 1: Temperature. S. Levitus,
706 Ed. NOAA Atlas NESDIS 68, U.S. Government Printing Office, Washington, D.C., 184 pp.

707 Manabe, S., and R. J. Stouffer, 1993: Century-scale effects of increased atmospheric CO_2 on the
708 ocean-atmosphere system, *Nature*, **364**, 215-218.

709 Middelburg, J. J., K. Soetaert, P. M. J. Herman, C. H. R. Heip, 1996: Denitrification in marine
710 sediments: A model study, *Glob. Biogeochem. Cycles*, **10**, 661-673, doi:10.1029/96GB02562.

711 Milly, P. C. D., and A. B. Shmakin, 2002: Global modeling of land water and energy balances. Part
712 I: The land dynamics (LaD) model. *J. Hydrometeorology*, **3**, 283-299.

713 Milly, P. C. D., et al., in preparation: Global modeling of land water and energy balances: The
714 land dynamics (LaD2) model. *J. Hydrometeorology*.

715 Moore, J.K., S. C. Doney, and K. Lindsay, 2004: Upper ocean ecosystem dynamics and iron cycling
716 in a global 3D model. *Global Biogeochem. Cycles*, **18**, GB4028, doi:10.1029/2004GB002220.

717 Najjar, R., and J. C. Orr (1998), Design of OCMIP-2 simulations of chlorofluorocarbons, the
718 solubility pump and common biogeochemistry, internal OCMIP report, 25 pp., LSCE/CEA Saclay,
719 Gif-sur-Yvette, France.

720 Najjar, R. G., X. Jin, F. Louanchi, O. Aumont, K. Caldeira, S. C. Doney, J. C. Dutay, M. Follows, N.
721 Gruber, F. Joos, K. Lindsay, E. Maier-Reimer, R. J. Matear, K. Matsumoto, P. Monfray, A. Mouchet,
722 J. C. Orr, G. K. Plattner, J. L. Sarmiento, R. Schlitzer, R. D. Slater, M. F. Weirig, Y. Yamanaka, and A.
723 Yool, 2007: Impact of circulation on export production, dissolved organic matter and dissolved
724 oxygen in the ocean: results from Phase II of the Ocean Carbon-cycle Model Intercomparison
725 Project (OCMIP-2). *Global Biogeochem. Cycles*, **21**, p. GB3007.

726 Olson, J. S., J. A. Watts, L. J. Allison, 1985: Major world ecosystem complexes ranked by carbon
727 in live vegetation: a database. Carbon Dioxide Information Center numerical Data Collection,
728 NDP-017, Oak Ridge, TN, DOI:10.3334/CDIAC/lue.ndp017.

729 Randall, D.A., R.A. Wood, S. Bony, R. Colman, T. Fichefet, J. Fyfe, V. Kattsov, A. Pitman, J. Shukla,
730 J. Srinivasan, R.J. Stouffer, A. Sumi and K.E. Taylor, 2007: Climate Models and Their Evaluation.

731 In: Climate Change 2007: The Physical Science Basis. Contribution of Working Group I to the
732 Fourth Assessment Report of the Intergovernmental Panel on Climate Change [Solomon, S., D.
733 Qin, M. Manning, Z. Chen, M. Marquis, K.B. Averyt, M.Tignor and H.L. Miller (eds.)]. Cambridge
734 University Press, Cambridge, United Kingdom and New York, NY, USA.

735 Randerson, J. T., M. V. Thompson, T. J. Conway, I. Y. Fung, and C. B. Field, 1997: The contribution
736 of terrestrial sources and sinks to trends in the seasonal cycle of atmospheric carbon dioxide.
737 *Global Biogeochem. Cycles*, **11**: 535-560.

738 Reichler, T., and J. Kim, 2008: How Well do Coupled Models Simulate Today's Climate? *Bull.*
739 *Amer. Meteor. Soc*., **89**, 303-311.

740 Sabine, C. L., R. A. Feely, N. Gruber, R. M. Key, K. Lee, J. L. Bullister,1 R. Wanninkhof, C. S. Wong,
741 D. W. R. Wallace, B. Tilbrook, F. J. Millero, T.-H. Peng, A. Kozyr, T. Ono, and A. F. Rios, 2004: The
742 Oceanic Sink for Anthropogenic CO_2. *Science*, **305**, 367-371.

743 Sarmiento, J.L. and C. Le Quéré, 1996: Oceanic carbon dioxide uptake in a model of century-
744 scale global warming. *Science*, **274**, 1346-1350.

745 Seitzinger, S. P., J. A. Harrison, E. Dumont, A. H. W. Beusen, and A. F. Bouwman, 2005: Sources
746 and delivery of carbon, nitrogen, and phosphorus to the coastal zone: An overview of Global
747 Nutrient Export from Watersheds (NEWS) models and their application, *Global Biogeochem.*
748 *Cycles*, **19**, GB4S01, doi:10.1029/2005GB002606.

749 Shevliakova, E., S. W. Pacala, S. Malyshev, P. C. D. Milly, and L. T Sentman, et al., 2009: Carbon
750 cycling under 300 years of land use change: Importance of the secondary vegetation sink.
751 Global Biogeochemical Cycles, 23, GB2022, doi:10.1029/2007GB003176.

752 Siegenthaler, U., and J. L. Sarmiento, 1993: Atmospheric carbon dioxide and the ocean. *Nature*,
753 **365**, 119-125.

754 Steinacher, M., F. Joos, T. L. Frölicher, L. Bopp, P. Cadule, V. Cocco, S. C. Doney, M. Gehlen, K.
755 Lindsay, J. K. Moore, B. Schneider, J. Segschneider, 2010: Projected 21st century decrease in
756 marine productivity: a multi-model analysis, *Biogeosciences*, **7**, 979-1005.

757 Stouffer, R. J., A. J. Weaver, and M. Eby, 2004: A method for obtaining pre-twentieth century
758 initial conditions for use in climate change studies. *Climate Dynamics*, **23**, 327-339.

759 Sunda, W. G. and S. A. Huntsman, 1997: Interrelated influence of iron, light and cell size on
760 marine phytoplankton growth. *Nature*, **390**, 389-392.

761 Takahashi T., S. C. Sutherland, R. Wanninkhof, C. Sweeney, R. A. Feely, D. W. Chipman, B. Hales,
762 G. Friederich, F. Chavez, C. Sabine, A. Watson, D. C.E. Bakker, U. Schuster, N. Metzl, H.
763 Yoshikawa-Inoue, M. Ishii, T. Midorikawa, Y. Nojiri, A. Körtzinger, T. Steinhoff, M. Hoppema, J.
764 Olafsson, T. S. Arnarson, B. Tilbrook, T. Johannessen, A. Olsen, R. Bellerby, C.S. Wong, B. Delille,
765 N.R. Bates, and H. J.W. de Baar :2009 Climatological mean and decadal change in surface ocean
766 pCO2, and net sea–air CO2 flux over the global oceans. *Deep-Sea Res. II*, **56**, 554-577.

767 Taylor, K.E., R.J. Stouffer, G.A. Meehl, 2011: An Overview of CMIP5 and the experiment design."
768 *Bull. Amer. Meteor. Soc*., doi:10.1175/BAMS-D-11-00094.1.

769 Thornton, P. E., J.-F. Lamarque, N. A. Rosenbloom, and N. M. Mahowald (2007), Influence of
770 carbon-nitrogen cycle coupling on land model response to CO2 fertilization and climate
771 variability, Global Biogeochem. Cycles, 21, GB4018, doi:10.1029/2006GB002868.

772 Ward, B.B., R.J. Olson, and M. J. Perry, 1982: Microbial nitrification rates in the primary nitrite
773 maximum off Southern California. *Deep-Sea Res.,* **29**, 247-255.

774 Welp, L. R., R. K. Keeling, H. A. J. Meijer, A. F. Bollenbacher, S. C. Piper, K. Yoshimura, R. J.
775 Francey, C.E. Allison, and M. Wahlen, 2011: Interannual variability in the oxygen isotopes of
776 atmospheric CO_2 driven by El Niño, *Nature*, **477**, 579-582.

777 Figures:

778 Figure 1: Global carbon cycle schematic comparison to estimate by Siegenthaler and Sarmiento
779 (1993) with ocean additions from IPCC; Sabine et al., 2004).

780 Figure 2: Globally averaged time series CO_2 fluxes across the atmosphere-land and atmosphere-
781 ocean interface. The initial conditions (t=0) are taken from prior atmosphere-only and ocean-
782 only integrations and radiative forcing is held constant at 1860 values (see Initialization section
783 for more details). Red lines indicate value from ESM2M, green ESM2G. (A) Annual Air-Sea CO_2
784 flux into ocean in units of PgC/yr. (B) Integrated Air-Sea CO_2 flux into ocean in PgC. (C) Ocean DIC
785 Inventory in units of Eg C. (D) Ocean ALK Inventory in units of EgC equivalent units. (E) Ocean
786 NO_3 Inventory in units of PgN.

787 Figure 3: Sea surface nitrate (NO_3; top row; µM), chlorophyll (Chl.; upper middle row; µg kg^{-1}),
788 air-sea carbon dioxide gas disequilibrium (ΔpCO_2; ppm; lower middle row), and phosphate (PO_4;
789 bottom row; µg kg^{-1}). In each case, the left column is an observational estimate while middle
790 (ESM2M) and right (ESM2G) columns are the model values. NO_3 and PO_4 observations are from
791 the World Ocean Altas 2009 (Garcia et al., 2010b;
792 http://www.nodc.noaa.gov/OC5/WOA09/pr_woa09.html), SeaWiFS chlorophyll from monthly
793 mapped level-3 concentration data for 1998-2007 (Reprocessing 2009;
794 http://oceandata.sci.gsfc.nasa.gov), and ΔpCO_2 from the 2006a reprocessing of Takahashi et al
795 (2009). On the model maps are plotted the bias, correlation coefficient and standard error
796 between the model and observationally based fields.

797 Figure 4: maps of ocean 500 m dissolved oxygen (O_2; top row; µM), phosphate (PO_4; middle
798 row; µM) and nitrate (NO_3; bottom row; µM). In each case, the left column is an observational
799 estimate while middle (ESM2M) and right (ESM2G) columns are the model derived values.
800 Observations are from the World Ocean Altas 2009 (Garcia et al., 2010a; Garcia et al., 2010b;
801 http://www.nodc.noaa.gov/OC5/WOA09/pr_woa09.html). On the model maps are plotted the
802 bias, correlation coefficient and standard error between the model and observationally based
803 fields.

804 Figure 5: Average vertical profiles of dissolved inorganic carbon (DIC; solid) and excess alkalinity
805 (ALK-DIC; dash) in µmol kg^{-1} for the (A) North Atlantic, (B) Tropics, (C) North Pacific and (D)
806 Southern Ocean for observations corrected to preindustrial values (Key et al., 2004; black),
807 ESM2M (red) and ESM2G (green).

808 Figure 6: Maps of vertically integrated total primary productivity (A-C; mol C m^{-2} a^{-1}), primary
809 productivity from large phytoplankton alone (D-F; mol C m^{-2} a^{-1}) and nitrogen fixation rates (G-I;
810 mol N m^{-2} a^{-1}) in the upper 100 m from ESM2M (A, D, G), ESM2G (B, E, H) and the difference (C,
811 F, I).

812 Figure 7: Zonal integral comparison of various metric of the biological (A; PgC a^{-1} deg^{-1}) and
813 mineral (B; PgC a^{-1} deg^{-1}) pumps in the upper 100 m for ESM2M (solid) and ESM2G (dashed).

814 Figure 8: Maps of species type (A-C), above-ground biomass (D-F; kgC m^{-2}), and climatological
815 maximum (G-I) and minimum (J-L) full spectrum Normalized Difference Vegetation Index (NDVI),
816 and. In each case, the left column is an observational estimate while middle (ESM2M) and right
817 (ESM2G) columns are the model derived values. Observations for vegetation type and biomass

818 are from Gibbs (2006) based on Olson et al. (1985) climate types obtained from the Carbon
819 Dioxide Information Center, Oak Ridge National Laboratory, Oak Ridge, Tennessee
820 (http://cdiac.ornl.gov/ftp/ndp017). NDVI observations are from Moderate Resolution Imaging
821 Spectroradiometer (MODIS) data.

822 Figure 9: Maps of ESM2M (A, C, E, G) and ESM2G (B, D, F, H) CO_2 flux mean (A, B; mol m^{-2} a^{-1}),
823 variability as the standard deviation of monthly mean values (C, D; mol m^{-2} a^{-1}), percentage of
824 that variability that is associated with the seasonal cycle rather than interannual modes (E, F;
825 %), and correlations of CO_2 flux variability with surface temperature.

826 Figure 10: Zonally integrated air-sea flux (A) of heat downward (dash; PW deg^{-1}) and CO_2
827 upward (solid; PgC a^{-1} deg^{-1}), and implied ocean transport (B) of heat northward (dash; PW) of
828 CO_2 southward (solid; PgC a^{-1}) for ESM2M (red) and ESM2G (green).

829 Figure 11: Maps of long term average surface atmospheric CO_2 anomalies from the global mean
830 (ppm; A, B), maps of squared correlation coefficient with the temporal variability in the annual
831 global average (C, D) and plots of the variability of annual average CO_2 (E, F) at Greenland
832 (black) and Antarctica (blue) for ESM2M (A, C, E) and ESM2G (B, D, F).

833 Figure 12: Amplitude of the seasonal cycle in CO_2 over marine stations compared to
834 observations, along with insets of the CO_2 wavelet spectra compared to observations from long
835 term monitoring stations at Barrow, Mauna Loa, and the South Pole. Note differing scale of
836 Barrow to the others. Data courtesy of NOAA's Global Monitoring Division's Carbon Cycle
837 Greenhouse Gases Group (http://www.esrl.noaa.gov/gmd/ccgg/index.html).

838

839 Figure 1:

840

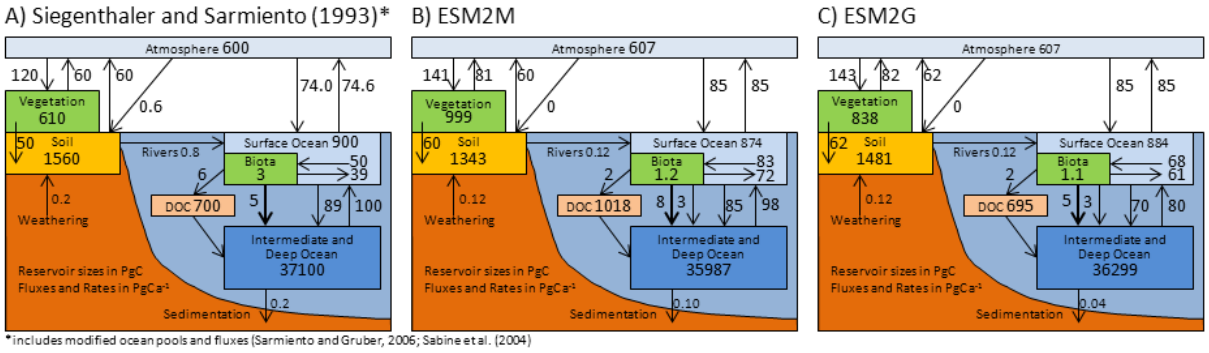

841

842 Figure 1: Global carbon cycle schematic comparison to estimate by Siegenthaler and Sarmiento

843 (1993) with ocean additions from IPCC; Sabine et al., 2004).

844

Figure 2:

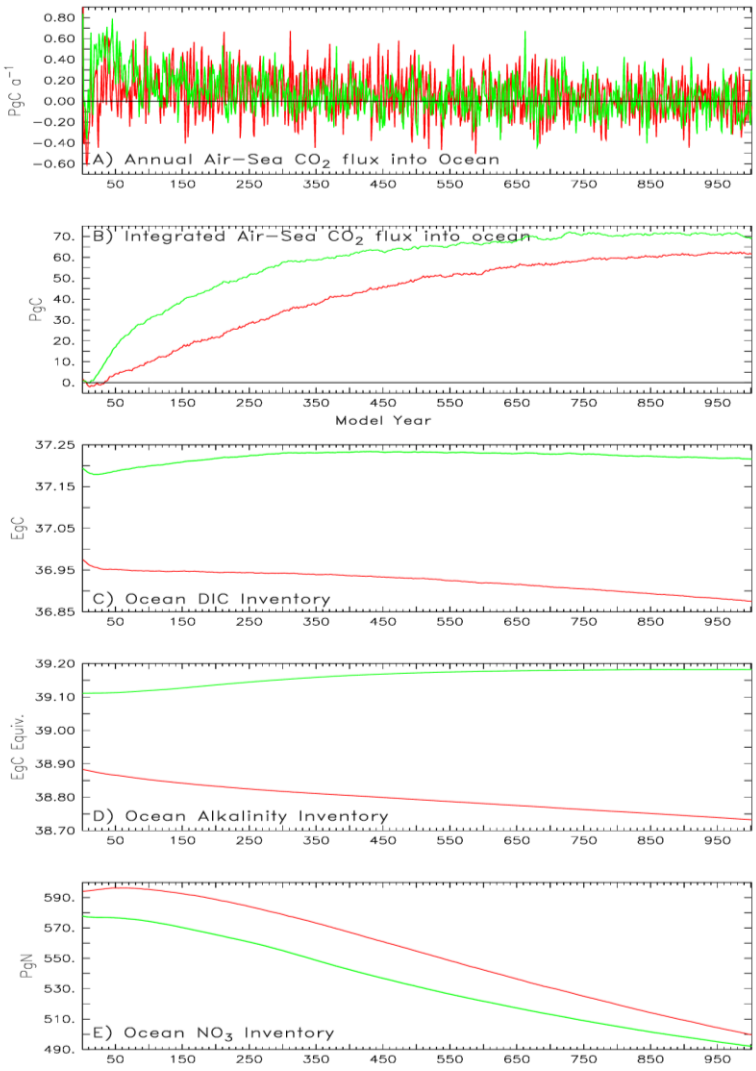

Figure 2: Globally averaged time series CO_2 fluxes across the atmosphere-land and atmosphere-ocean interface. The initial conditions (t=0) are taken from prior atmosphere-only and ocean-only integrations and radiative forcing is held constant at 1860 values (see Initialization section for more details). Red lines indicate value from ESM2M, green ESM2G. (A) Annual Air-Sea CO_2 flux into ocean in units of PgC/yr. (B) Integrated Air-Sea CO_2 flux into ocean in PgC. (C) Ocean DIC Inventory in units of Eg C. (D) Ocean ALK Inventory in units of EgC equivalent units. (E) Ocean NO_3 Inventory in units of PgN.

Figure 3:

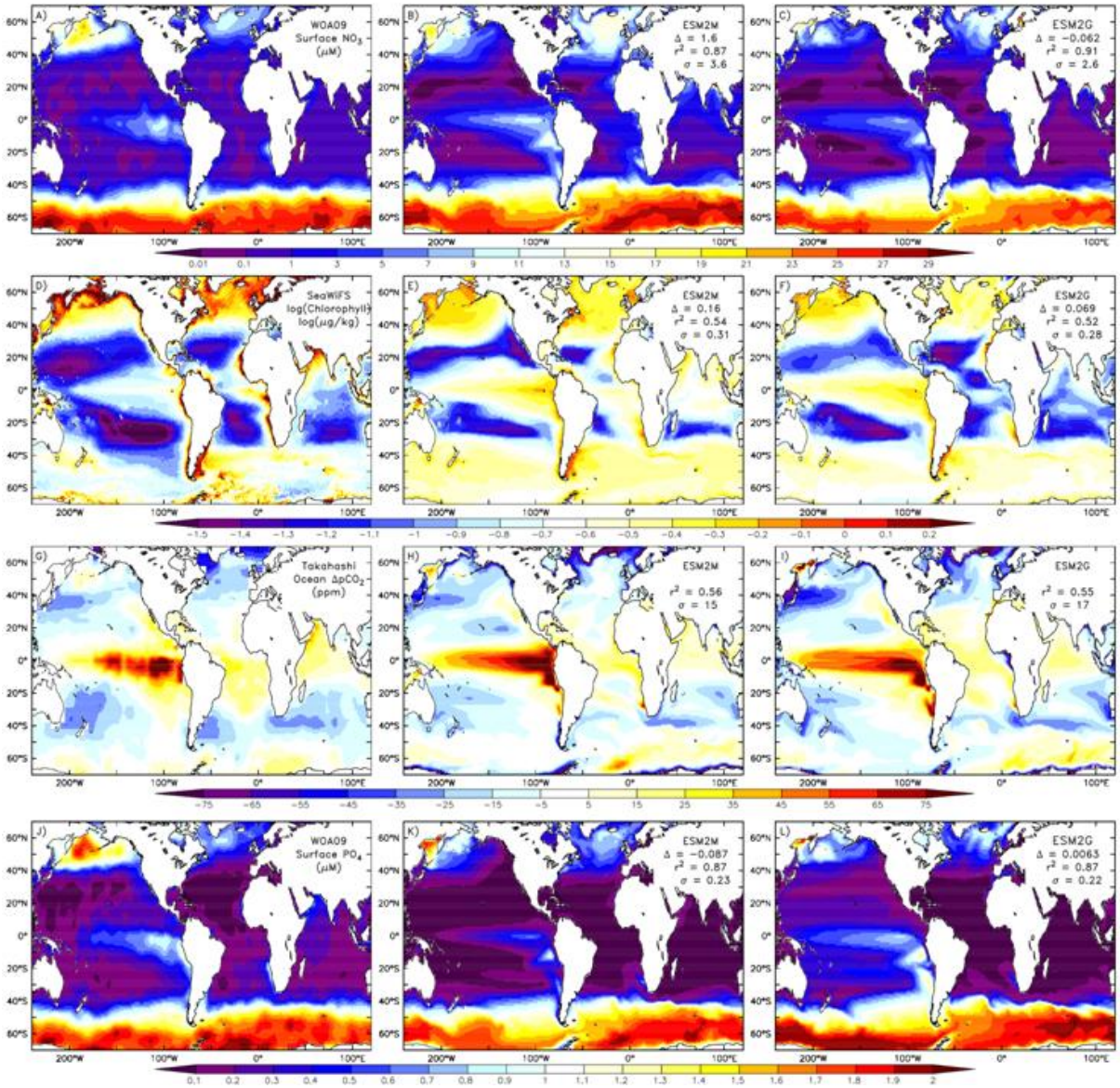

Figure 3: Sea surface nitrate (NO_3; top row; µM), chlorophyll (Chl.; upper middle row; µg kg^{-1}), air-sea carbon dioxide gas disequilibrium (ΔpCO_2; ppm; lower middle row), and phosphate (PO_4; bottom row; µg kg^{-1}). In each case, the left column is an observational estimate while middle (ESM2M) and right (ESM2G) columns are the model values. NO_3 and PO_4 observations are from the World Ocean Altas 2009 (Garcia et al., 2010b;

861 http://www.nodc.noaa.gov/OC5/WOA09/pr_woa09.html), SeaWiFS chlorophyll from monthly
862 mapped level-3 concentration data for 1998-2007 (Reprocessing 2009;
863 http://oceandata.sci.gsfc.nasa.gov), and ΔpCO_2 from the 2006a reprocessing of Takahashi et al
864 (2009). On the model maps are plotted the bias, correlation coefficient and standard error
865 between the model and observationally based fields.

866

867 Figure 4:

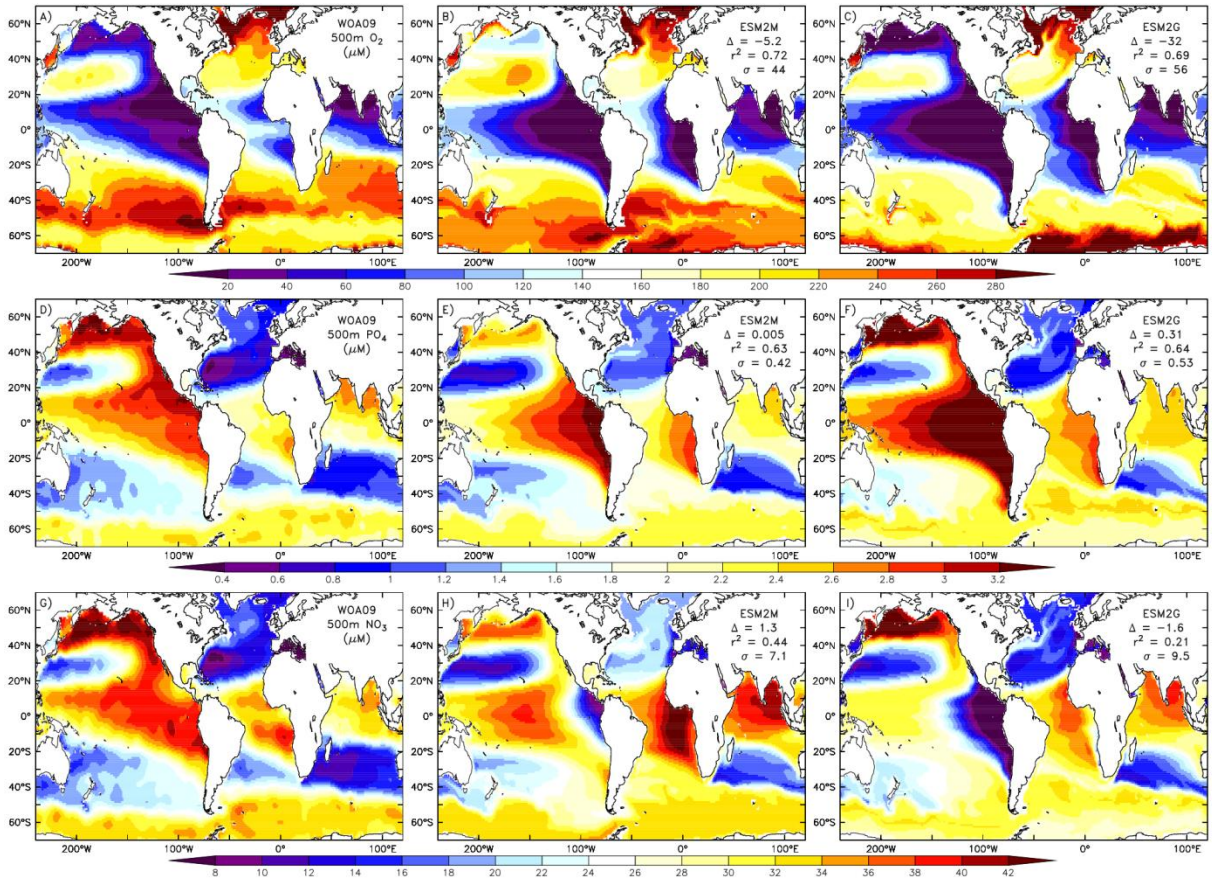

868

869 Figure 4: maps of ocean 500 m dissolved oxygen (O_2; top row; μM), phosphate (PO_4; middle
870 row; μM) and nitrate (NO_3; bottom row; μM). In each case, the left column is an observational
871 estimate while middle (ESM2M) and right (ESM2G) columns are the model derived values.
872 Observations are from the World Ocean Altas 2009 (Garcia et al., 2010a; Garcia et al., 2010b;
873 http://www.nodc.noaa.gov/OC5/WOA09/pr_woa09.html). On the model maps are plotted the
874 bias, correlation coefficient and standard error between the model and observationally based
875 fields.

876 Figure 5:

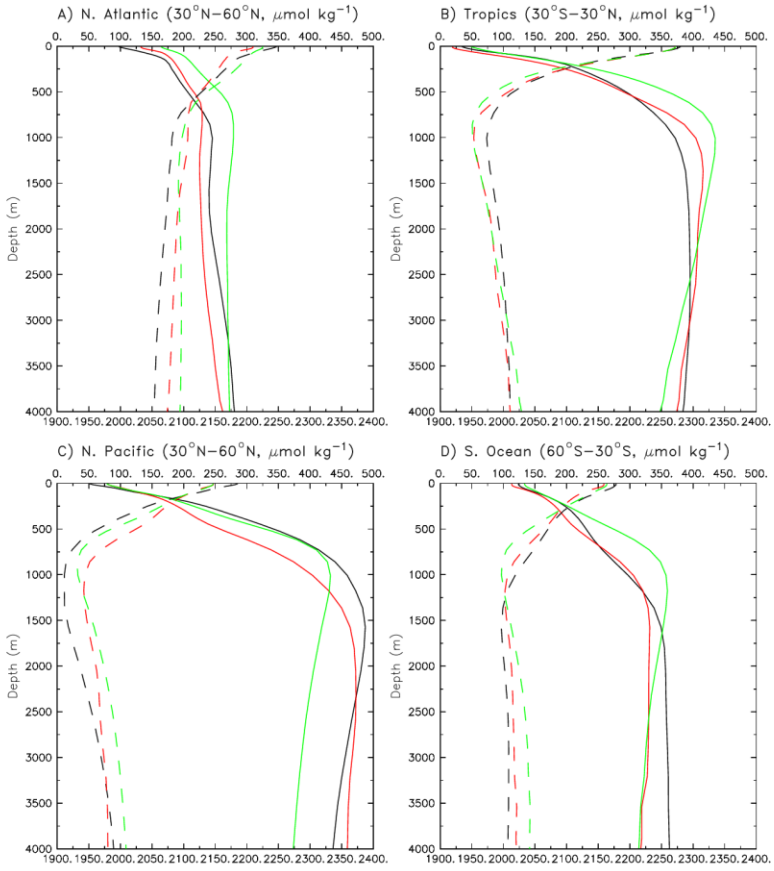

877

878 Figure 5: Average vertical profiles of dissolved inorganic carbon (DIC; solid) and excess alkalinity

879 (ALK-DIC; dash) in µmol kg^{-1} for the (A) North Atlantic, (B) Tropics, (C) North Pacific and (D)

880 Southern Ocean for observations corrected to preindustrial values (Key et al., 2004; black),

881 ESM2M (red) and ESM2G (green).

882

883 Figure 6:

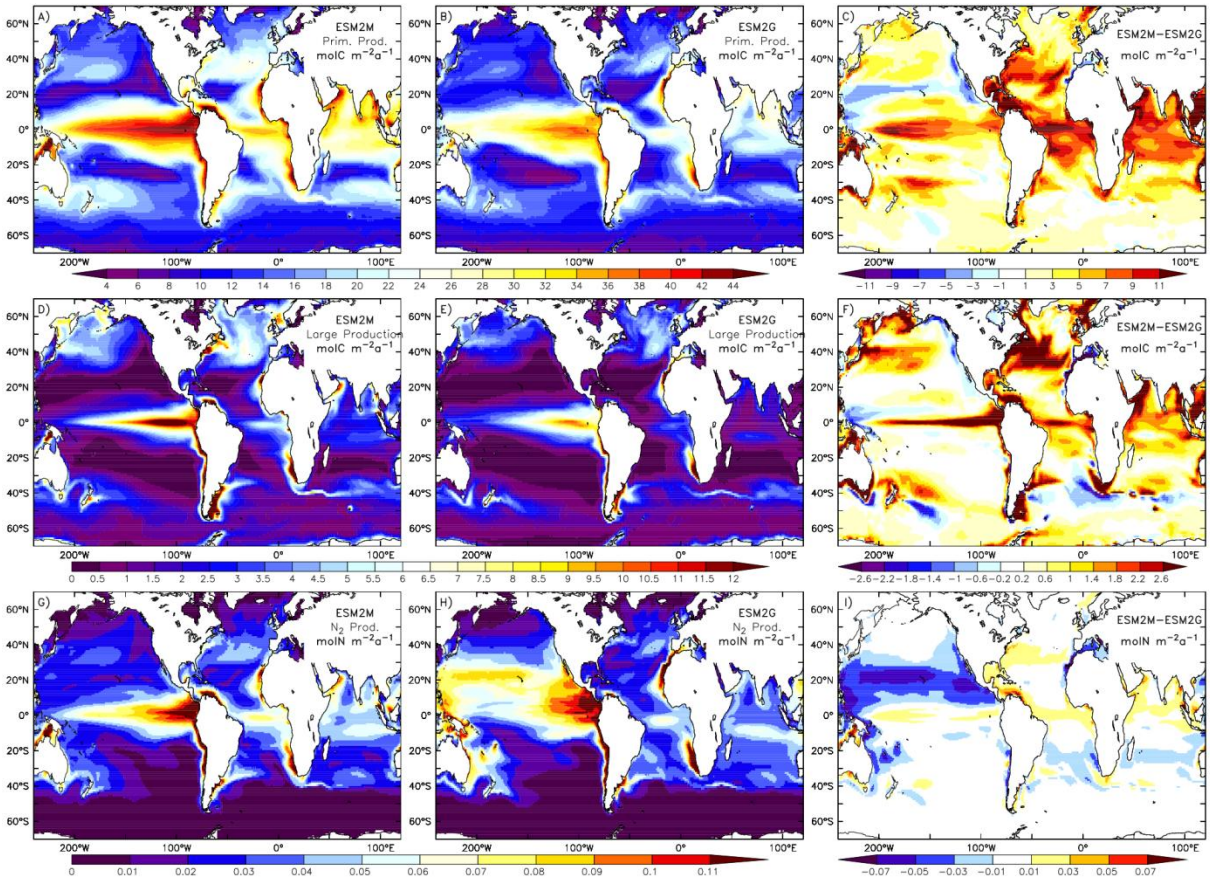

884

885 Figure 6: Maps of vertically integrated total primary productivity (A-C; mol C m^{-2} a^{-1}), primary

886 productivity from large phytoplankton alone (D-F; mol C m^{-2} a^{-1}) and nitrogen fixation rates (G-I;

887 mol N m^{-2} a^{-1}) in the upper 100 m from ESM2M (A, D, G), ESM2G (B, E, H) and the difference (C,

888 F, I).

889

890

891 Figure 7:

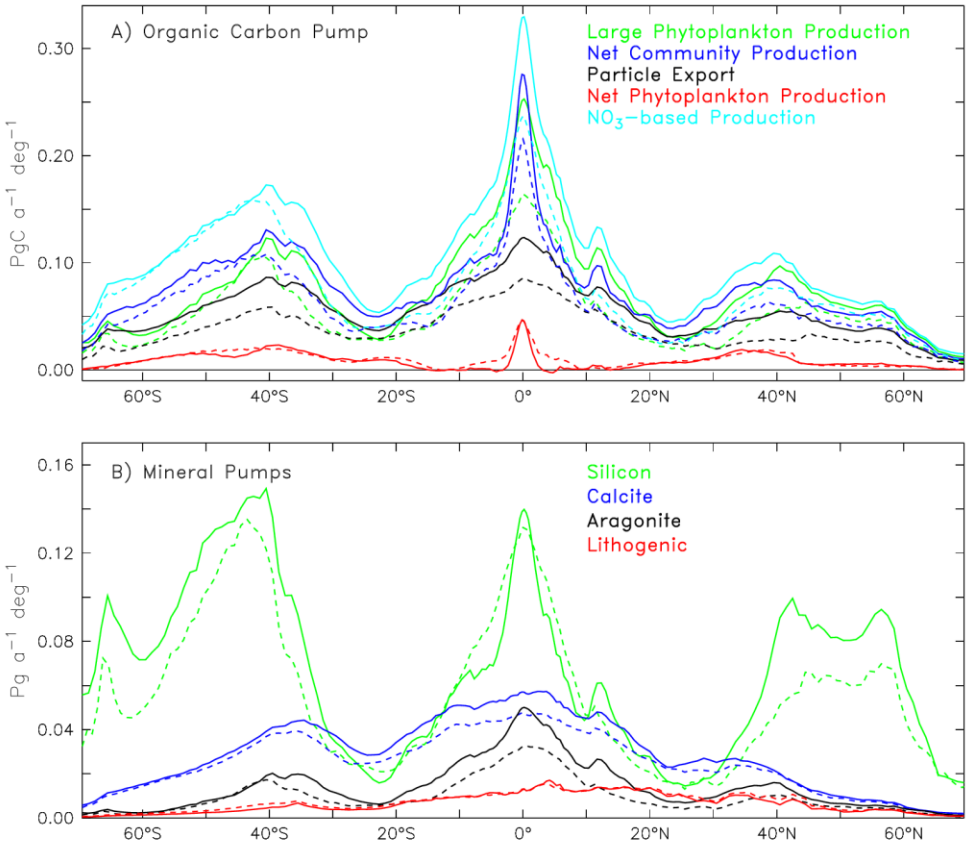

892

893 Figure 7: Zonal integral comparison of various metric of the biological (A; PgC a^{-1} deg^{-1}) and

894 mineral (B; PgC a^{-1} deg^{-1}) pumps in the upper 100 m for ESM2M (solid) and ESM2G (dashed).

895

Figure 8:

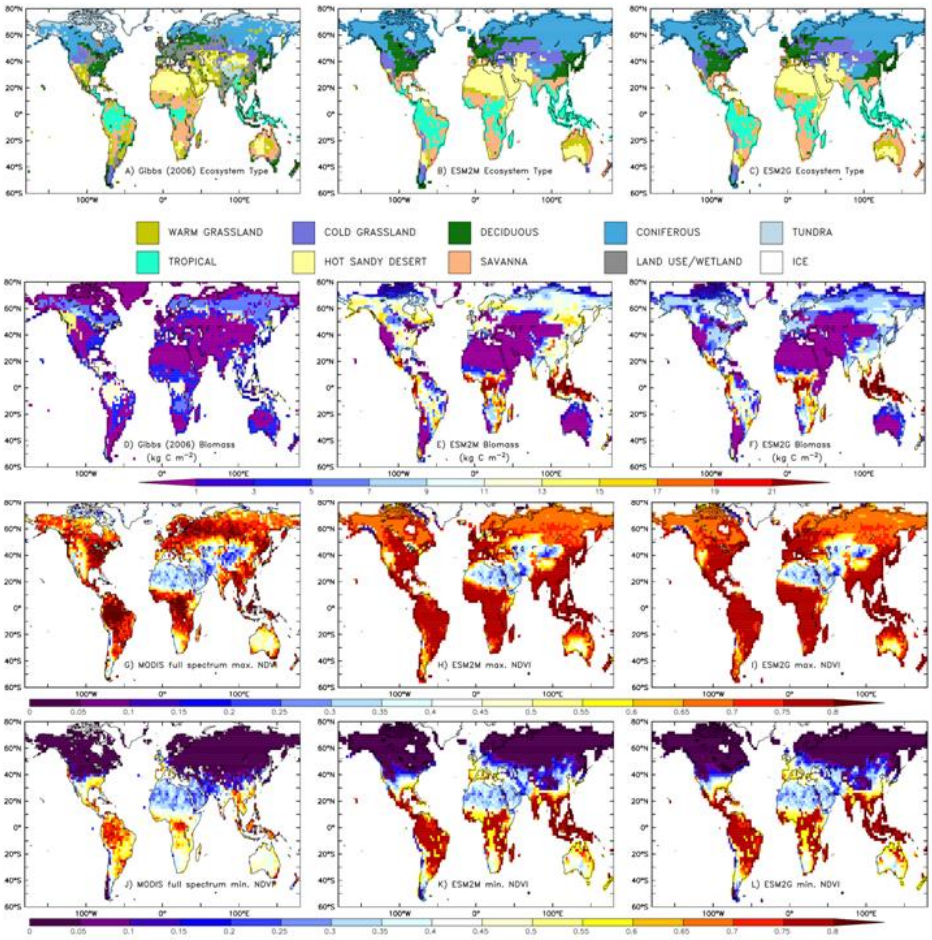

Figure 8: Maps of species type (A-C), above-ground biomass (D-F; kgC m^{-2}), and climatological maximum (G-I) and minimum (J-L) full spectrum Normalized Difference Vegetation Index (NDVI), and. In each case, the left column is an observational estimate while middle (ESM2M) and right (ESM2G) columns are the model derived values. Observations for vegetation type and biomass are from Gibbs (2006) based on Olson et al. (1985) climate types obtained from the Carbon Dioxide Information Center, Oak Ridge National Laboratory, Oak Ridge, Tennessee (http://cdiac.ornl.gov/ftp/ndp017). NDVI observations are from Moderate Resolution Imaging Spectroradiometer (MODIS) data.

906 Figure 9:

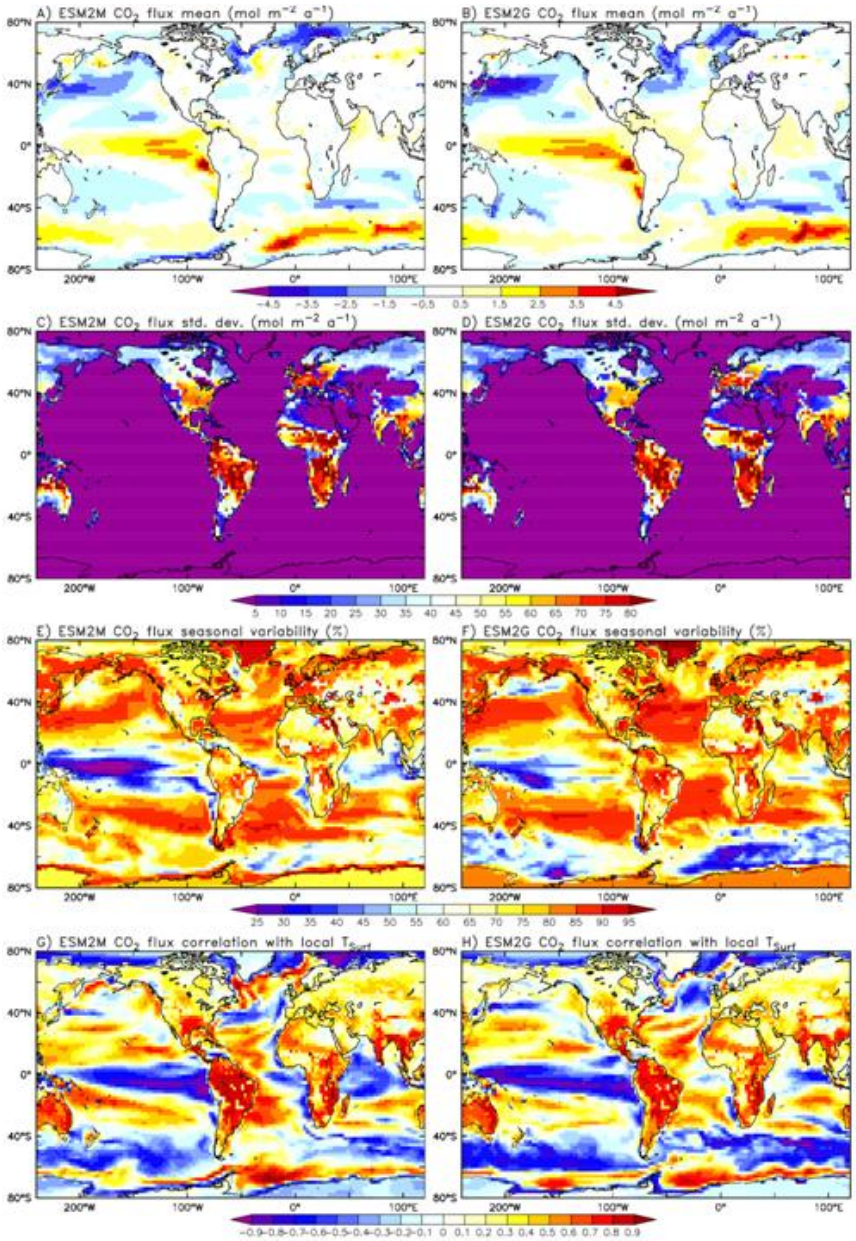

907

908 Figure 9: Maps of ESM2M (A, C, E, G) and ESM2G (B, D, F, H) CO_2 flux mean (A, B; mol m^{-2} a^{-1}),

909 variability as the standard deviation of monthly mean values (C, D; mol m^{-2} a^{-1}), percentage of

910 that variability that is associated with the seasonal cycle rather than interannual modes (E, F;

911 %), and correlations of CO_2 flux variability with surface temperature.

912 Figure 10:

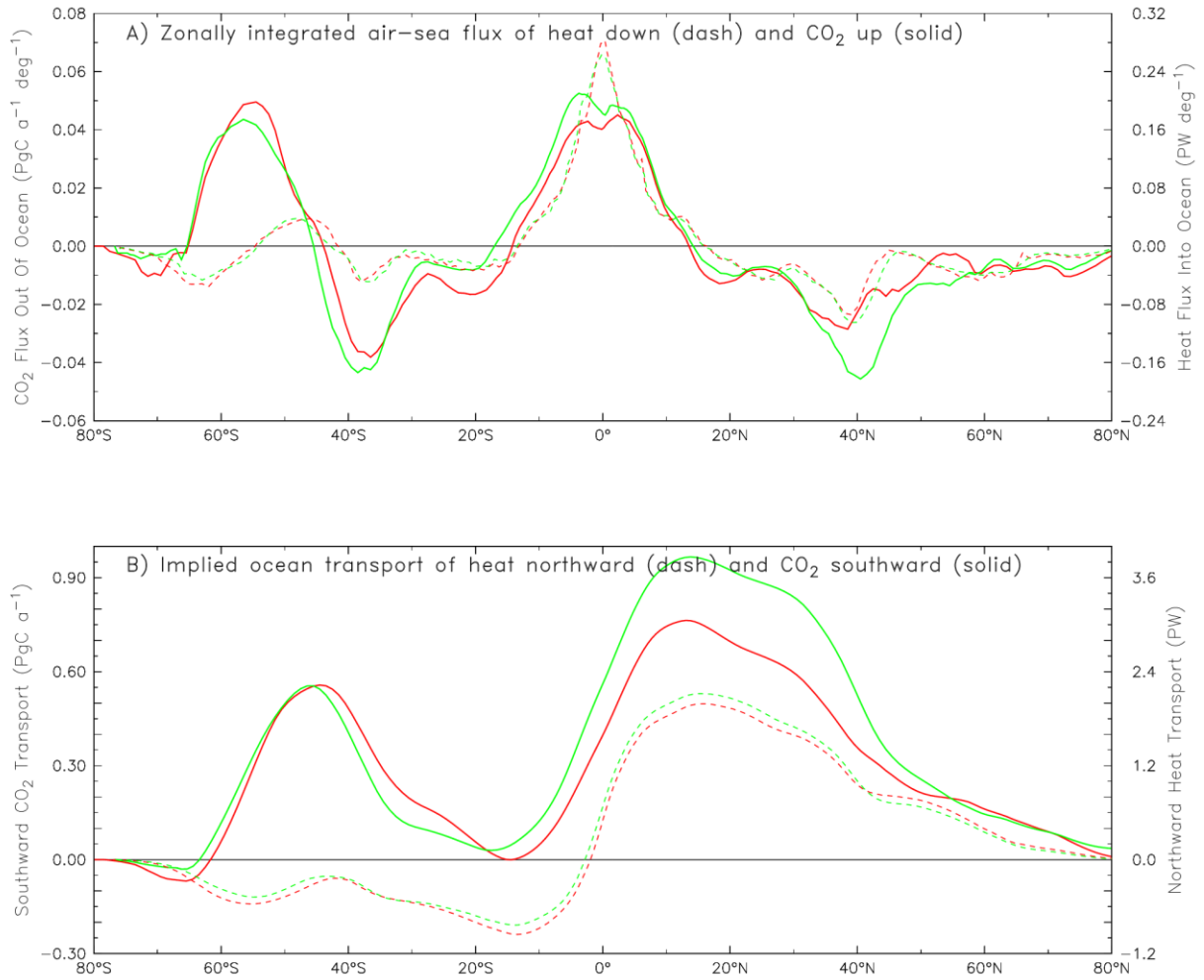

913

914 Figure 10: Zonally integrated air-sea flux (A) of heat downward (dash; PW deg^{-1}) and CO_2

915 upward (solid; PgC a^{-1} deg^{-1}), and implied ocean transport (B) of heat northward (dash; PW) of

916 CO_2 southward (solid; PgC a^{-1}) for ESM2M (red) and ESM2G (green).

917

Figure 11:

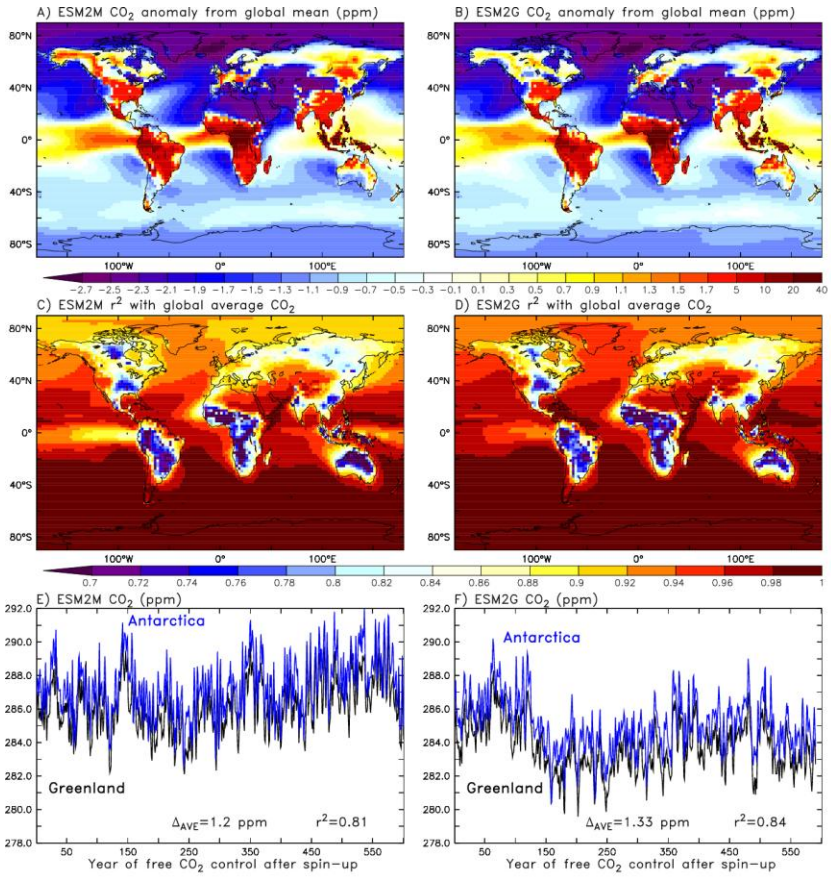

Figure 11: Maps of long term average surface atmospheric CO_2 anomalies from the global mean (ppm; A, B), maps of squared correlation coefficient with the temporal variability in the annual global average (C, D) and plots of the variability of annual average CO_2 (E, F) at Greenland (black) and Antarctica (blue) for ESM2M (A, C, E) and ESM2G (B, D, F).

925 Figure 12:

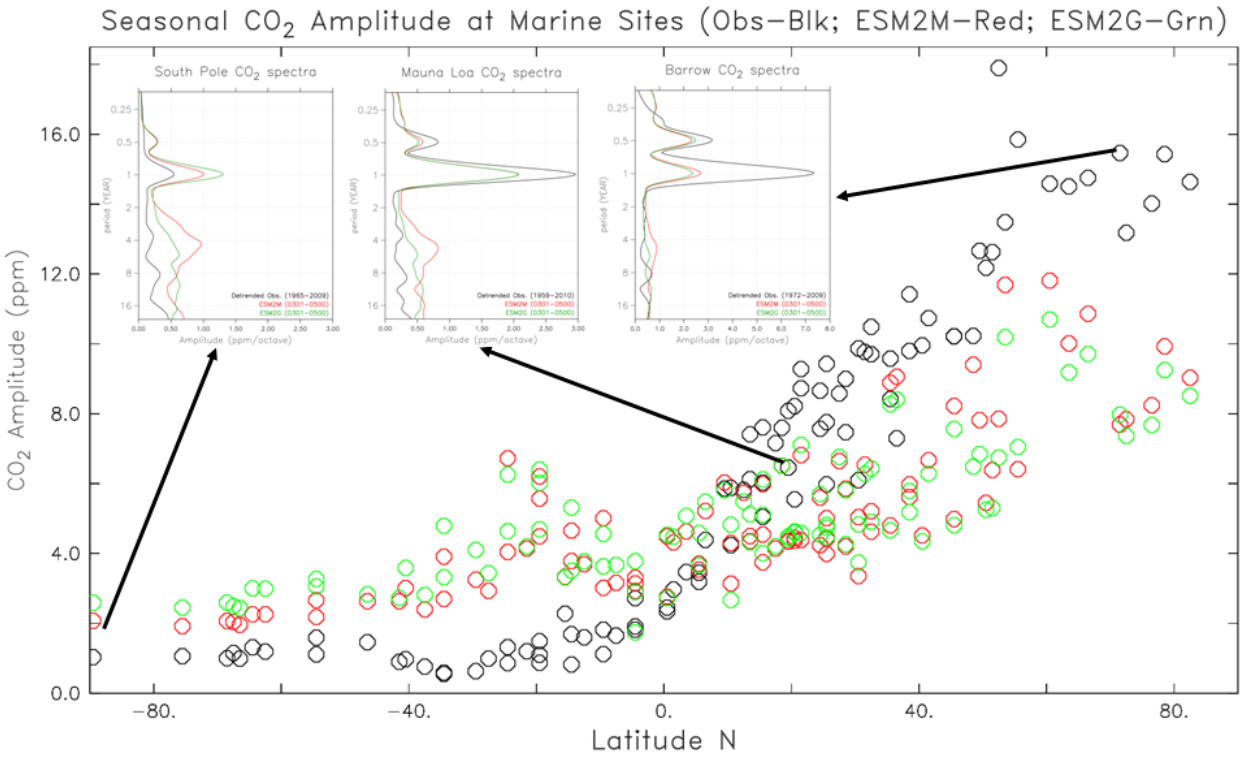

926

927 Figure 12: Amplitude of the seasonal cycle in CO_2 over marine stations compared to

928 observations, along with insets of the CO_2 wavelet spectra compared to observations from long

929 term monitoring stations at Barrow, Mauna Loa, and the South Pole. Note differing scale of

930 Barrow to the others. Data courtesy of NOAA's Global Monitoring Division's Carbon Cycle

931 Greenhouse Gases Group (http://www.esrl.noaa.gov/gmd/ccgg/index.html).

932

Non-Rendered Figure
Click here to download Non-Rendered Figure: carbon_cycle_comparison_big.png

Non-Rendered Figure
Click here to download Non-Rendered Figure: global_dic_stf_ts_plots.png

Non-Rendered Figure
Click here to download Non-Rendered Figure: surface_NCchlCO2P.png

Non-Rendered Figure
Click here to download Non-Rendered Figure: fig4_SSN_500mO2_P_N.png

Non-Rendered Figure
Click here to download Non-Rendered Figure: dic_comparison_v3.png

Non-Rendered Figure
Click here to download Non-Rendered Figure: pp_lpp_nfix.png

Non-Rendered Figure
Click here to download Non-Rendered Figure: zonal_surface_bgc.png

Non-Rendered Figure
Click here to download Non-Rendered Figure: vegtype_biomass_ndvi.png

Non-Rendered Figure
Click here to download Non-Rendered Figure: co2_flux_mean_var_seas_corr.png

Non-Rendered Figure
Click here to download Non-Rendered Figure: poleward_co2_flux_1860.png

Non-Rendered Figure
Click here to download Non-Rendered Figure: co2_atm_maps.png

Non-Rendered Figure
Click here to download Non-Rendered Figure: co2_amplitude.png